
# A MIGHTEE Investigation of Radio Quiet AGN

*A thesis submitted in fulfillment of the academic requirements for the degree of*

**MASTER OF SCIENCE**

*in the Department of Physics and Electronics*

**Author:** Neo Namane
**ORCID ID:** 0000-0001-5234-1243

**Supervisor:** Oleg Mikhailovich Smirnov
**Co-supervisor:** Sarah Virginia White

**Date:** 28 June 2023

**Declaration**

I, Neo Namane, hereby declare that this thesis titled "A MIGHTEE investigation of radio quiet AGN" is my original contribution. I confirm that:

1. This work has not been previously submitted for any degree or examination at any other institution.
2. The sources of information used and cited in this thesis have been appropriately acknowledged.
3. Any assistance received in the preparation of this thesis and any sources of funding have been acknowledged.
4. This thesis is the result of my own research and efforts, with guidance from my supervisors.
5. I have complied with the ethical guidelines and regulations applicable to my field of study.
6. I understand that any breach of academic integrity, including plagiarism, may result in severe consequences.

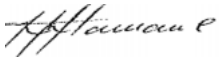

*Neo Namane*

Date: 28 June 2023

**Acknowledgements**

I would like to express my deepest gratitude and appreciation to all those who have supported and contributed to the completion of this MSc thesis.

First and foremost, I am grateful to my supervisors, Oleg and Sarah, for their guidance, expertise, and invaluable support throughout this research project. Their knowledge and insights have been instrumental in shaping this thesis.

I would like to thank the members of my research group and colleagues at Rhodes University for their stimulating discussions and assistance throughout my MSc studies. Their contributions have enriched my understanding and helped me overcome challenges encountered during this research journey.

I am indebted to the South African Radio Astronomy Observatory for providing the financial support. Their funding has enabled me to conduct this research and access necessary resources, greatly contributing to the successful completion of this thesis.

I would also like to express my appreciation to the staff and faculty members of the Department of Physics and Electronics at Rhodes for their guidance, resources, and the conducive academic environment they have created.

Furthermore, I extend my gratitude to my family and friends for their unwavering support, encouragement, and belief in my abilities. Their love and understanding have been invaluable throughout this journey.

Lastly, I would like to acknowledge all the researchers, authors, and scientists whose work and publications have served as a foundation for my research. Their contributions have played a significant role in shaping my understanding and findings.

In conclusion, I am grateful to everyone who has played a part, big or small, in this research endeavor. Your support, encouragement, and contributions have been indispensable, and I am truly grateful for the opportunity to undertake this MSc thesis in Physics. Special thanks is extended to Sam Altman and collaborators for their creation of the ChatGPT platform which was instrumental in helping construct this thesis. The technology's performance has indeed proven that: this technology is a step towards building "artificial general intelligence" that "benefits all of humanity" [Kasirzadeh, 2023]. In the course of this research, I used ChatGPT as a supplementary tool for specific tasks, that include assistance in calculations, code generation, and sentence construction. It is important to note that while ChatGPT provided valuable assistance, the intellectual content, analysis, and conclusions presented in this thesis are solely the result of the independent research efforts of Sarah, Oleg, myself, and the two external examiners appointed to evaluate the quality of this work. I would also be greatly misled in not acknowledging the Tshimologong Digital Innova-

tion Precinct for assisting with the necessary internet access required to complete the final stages of the completion of this piece of literature. This acknowledgement aims to maintain transparency regarding the tools employed in the research process, ensuring adherence to principles of academic integrity.

**Abstract**

This study is aimed at being an overview and investigation of the behaviour and morphology of radio quiet (RQ) active galactic nuclei (AGN) in the radio and optical/near-infrared (NIR) bands. It is hoped that a concise description of the relation that exists between accretion activity and star formation (SF) will be achieved through utilization of multi-wavelength astronomy analysis. This analysis includes the processing of data acquired from the MeerKAT International GHz Tiered Extragalactic Exploration survey (MIGHTEE), the Southern African Large Telescope (SALT), the Hyper Suprime Camera (HSC) mounted on the Subaru telescope and the VISTA telescope. In this thesis, several targets were observed using SALT spectroscopy, but a redshift of only one of them was obtained. Lastly, it was established that for the sample of RQ AGN studied, the AGN contribute a large fraction of the radio emission observed.

**List of abbreviations:**

**AGN** - Active Galactic Nucleus (/Nuclei)
**CMB** - Cosmic Microwave Background
**HSC** - Hyper Suprime Cam
**IGM** - Inter-Galactic Medium
**IRRC** - InfraRed Radio Correlation
**ISM** - Inter-Stellar Medium
**LSPs** - Large Survey Projects
**MeerKAT** - "Meer" Karoo Array Telescope
**MIGHTEE** - MeerKAT International GigaHertz Tiered Extragalactic Exploration
**RLQ** - Radio Loud Quasar
**RQQ** - Radio Quiet Quasar
**RSS** - Robert Stobie Spectrograph
**SAAO** - South African Astronomy Observatory
**SALT** - Southern African Large Telescope
**SARAO** - South African Radio Astronomy Observatory
**SED** - Spectral Energy Distribution
**SF** - Star Formation
**SFG** - Star Forming Galaxy
**SFR** - Star Formation Rate
**SKA** - Square Kilometer Array

# Contents

# 1 Introduction

> "This is only a foretaste of what is to come, and only the shadow of what is going to be"
>
> Alan Turing, *£50 bank note*

The study of astronomy is essentially the observation and interpretation of numerous cosmic objects that are known in terms of their individual properties. A class of one of these partially understood objects are what are known as active galactic nuclei (AGN). These are essentially the optically luminous cores that are apparently driven by black hole (BH) activity and surrounding accretion that is found at the center of active galaxies. This thesis is aimed at investigating AGN and the role that they play in the contribution of radio luminosity to these galaxies. Using data acquired mainly from two South African telescopes - the Southern African Large Telescope (SALT) and the Meer [1] Karoo Array Telescope (MeerKAT), the spectral features and morphological attributes tied to a selection of AGN, are investigated. This is done so as to better determine whether radio luminosities are dominated by AGN activity over star formation (SF). To be more specific, this work aims to disentangle the confusion that exists within current literature around the dominant source of radio emission, namely between star forming regions and radio quiet quasar (RQQ) activity as contrastly demonstrated in Kimball et al. [2011] and White et al. [2015], respectively.

RQQs were initially identified in the mid-20th century during the early days of radio astronomy. Their discovery was propelled by advancements in radio telescopes, which allowed scientists to detect celestial objects emitting radio waves. Through the work of Jansky [1935] it was discovered that radiation is emitted by the whole disk of the Milky Way, and is strongest in the Galactic center's direction [Shields, 1999]. The mission of this thesis is twofold: first, to deepen our comprehension of AGN, and second, to cast clarity on the intricate interplay among AGN, SF and the radio luminosity that emanates from these RQQs. By studying AGN, we aim to untangle the complex astrophysical processes surrounding black holes and their accretion disks, which contribute to observed radio emissions. Understanding AGN has implications for cosmic evolution and the structure of galaxies.

[1] Meer is the Afrikaans word for more.

## 1.1 The Electromagnetic spectrum

The electromagnetic force is part of what is known as the four fundamental forces of nature. This force is produced as a result of the excitation of the electromagnetic field, wherein the simultaneous wave-like (see MacKinnon [1976] for an exposition of Louis de Broglie's thesis) and particle-like propagation of photons is induced. Within these propagations lie radio waves (long wavelength $\implies$ low frequency $\implies$ low energy output) all the way until gamma rays (short wavelength $\implies$ high frequency $\implies$ high energy output). Visible light forms part of this spectrum, and is

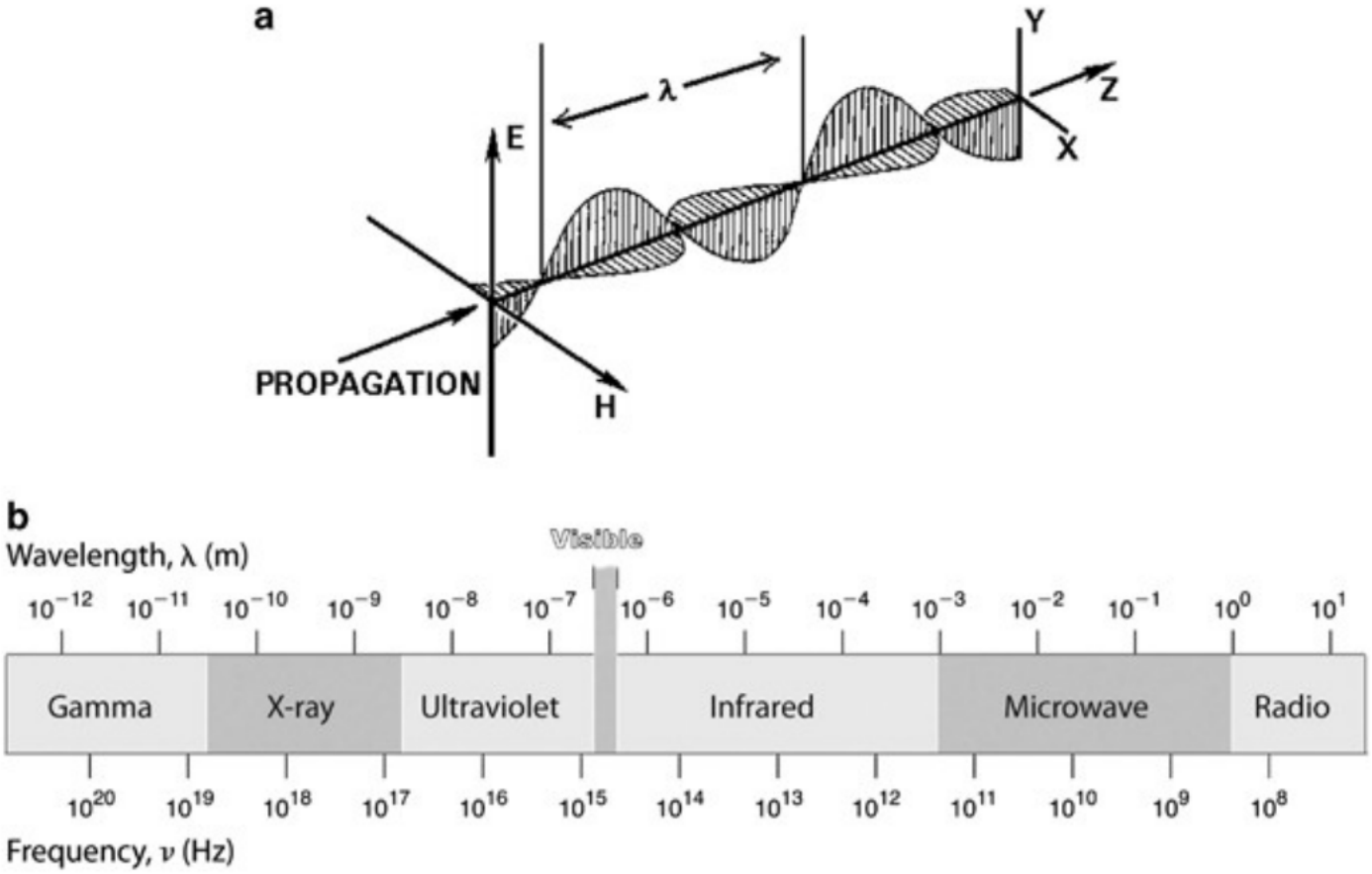


**Figure 1:** a) E and H represent the electric and subsequent magnetic field contributions. b) The electromagnetic spectrum. Images a) and b) are both extracted from Sliney [2016].

sometimes optically extinguished due to the existence of dust amongst some galaxies (see Roche et al. [1986] for an example). In order to deal with this problem, optical data can be enhanced with radio data tied to the same patch of sky so as to better compare observations of a particular entity. Combining optical data with radio data can be valuable for a variety of reasons in astronomy and astrophysics. The choice of using radio data over other types of data, such as X-ray or infrared

(IR) data, depends on the specific goals and characteristics of the observations. Here are some important reasons for incorporating radio data for our study's use case and why it might be preferred in certain cases:

- Multi-wavelength Perspective: Our investigation of radio quiet AGN relies on the integration of optical/NIR and radio data to discern the dominant source of radio emission between SF and AGN feedback activity.
- Penetration of Dust and Gas: The combined optical/NIR and radio data enable us to probe regions obscured by dust and gas, crucial for examining the interplay between SF and AGN feedback processes within radio quiet AGN.
- Magnetic Fields: Integrating optical/NIR and radio data enhances our sensitivity to magnetic fields, providing essential clues to differentiate between the contributions of SF and AGN activity.
- Synchrotron Emission: The synchrotron radiation detected across optical/NIR and radio wavelengths serves as a key indicator of both SF and AGN feedback activity, enriching our understanding of the underlying emission mechanisms.
- Extended Structures: Optical/NIR and radio observations allow for the detailed study of extended structures associated with AGN and star-forming regions, facilitating the identification of the dominant radio-emitting source within these environments.
- Galaxy Evolution and Cosmology: Our multi-wavelength approach enables us to situate RQ AGN within the broader context of galaxy evolution and cosmology, shedding light on their role in shaping large-scale structures and cosmic phenomena.
- Transient and Variable Sources: By monitoring transient and variable sources across optical/NIR and radio wavelengths, astronomers gain valuable insights into the dynamic nature of RQ AGN, essential for determining their prevailing emission mechanisms.
- Low Sensitivity to Interstellar Extinction: The combined optical/NIR and radio data mitigate the effects of interstellar extinction, allowing scientists to investigate regions with high extinction and uncover the characteristics of RQ AGN under challenging observational conditions.

An example of this is presented in Harrison et al. [2020], wherein radio and optical data from the SuperCLASS survey were used to verify weak gravitational lensing effects that are inherent within some radio emissions. Essentially, a comparison of any combination of frequency band observations

can be done, as exemplified in studies such as Joshi et al. [2020], where optical and X-ray studies of polars (cataclysmic variable binary stars) were conducted and Shirasaki et al. [2020] - where the cross correlation of the extragalactic $\gamma$-ray background with the thermal Sunyaev-Zel'dovich effect in the CMB was explored. This list even encompasses studies that include more than two frequency bands [Kennedy et al., 2020] - the optical, X-ray, and $\gamma$-ray observations of a candidate transitional millisecond pulsar.

The selection of specific frequency bands in this study, namely optical/NIR and radio, is meticulously guided by the study's distinct objectives:

- Scientific Objectives Alignment: The choice of bands directly corresponds to the objectives of our research. Optical/NIR and radio bands are particularly pertinent for quasar studies, as they unveil crucial insights into quasar properties, including the older stellar population of the host galaxy and the activity of radio jets.

- Consideration of Sensitivity and Resolution: Priority is given to bands based on the sensitivity and resolution of available instruments. Optical/NIR and radio bands offer superior capabilities for detecting faint or distant quasars and capturing intricate structural details with high fidelity.

- Mitigation of Atmospheric Interference: Given the significance of precise astronomical observations, we opt for bands less susceptible to atmospheric interference. Radio bands, in particular, remain impervious to atmospheric disturbances, ensuring the reliability of our data.

- Exploitation of Complementary Information: Each chosen band contributes unique and complementary data essential for a comprehensive understanding of quasars. While optical/NIR observations elucidate details regarding quasar accretion disks, radio observations unveil non-thermal processes.

Multi-wavelength astronomy comes with a lot of useful benefits in terms of observing and understanding the known Universe. As a result, studying the Universe at different wavelengths has given rise to incredible discoveries, from pulsars in the radio part of the electromagnetic spectrum and signatures of the Big Bang at submillimeter wavelengths, through to high energy emission from accreting, gravitationally-compact objects and the discovery of gamma-ray bursts, e.g. Middleton et al. [2017]. Coupled with recent gravitational wave detections that even inspire inquiry into the use of directly searching for inflationary gravitational waves [Smith et al., 2006], multi-wavelength astronomy holds the potential to further demystify our limited understanding of the full extent of

galactic dynamics and the subsequent evolution of the Universe as a whole. By combining data from multiple wavelengths, astronomers can paint a more complete picture of celestial objects and phenomena. This not only deepens our understanding, but also allows us to test and refine existing theories and models. Multi-wavelength observations can reveal unexpected connections and relationships between different cosmic processes, leading to new discoveries and insights that would be impossible to gain through single-wavelength observations alone. Essentially, it helps demystify the Universe by allowing us to explore and comprehend its many facets in greater detail.

### 1.1.1 Southern African Large Telescope (SALT)

SALT is an optical/NIR, ten-meter telescope [Stobie et al., 2000] located in the Sutherland - Northern Cape province. It is primarily based on the design of the Hobby-Eberly Telescope at the McDonald Observatory and is considered the largest optical/NIR telescope in the Southern Hemisphere. Its mirror spans an impressive 11.1 by 9.8 meters, enabling high-resolution imaging and spectroscopy. Situated at an elevation of 1798 meters, SALT remains fixed at an elevation angle of 53 degrees. Construction of SALT commenced in 2000, and it began observing the skies in 2005, marking a significant milestone in the pursuit of astronomical exploration.

SALT is at the forefront of cutting-edge astronomical research and has played a vital role in numerous groundbreaking discoveries. Its capabilities extend beyond traditional optical telescopes, incorporating innovative technologies such as adaptive optics systems and specialized spectrographs. These features enable SALT to investigate a wide range of celestial phenomena, including distant galaxies, quasars, supernovae, and BHs. Moreover, SALT stands as a testament to international collaboration, with multiple institutions and countries joining forces to bring this remarkable scientific endeavor to fruition. The collective efforts of astronomers and engineers from around the world have made SALT an invaluable asset in unraveling the mysteries of the Universe.

### 1.1.2 Spectroscopy

Spectroscopy is a powerful tool that allows scientists to gain profound insights into the nature of celestial objects. By analyzing the emission and absorption of visible electromagnetic radiation, spectroscopy unveils a wealth of information about an entity's properties. This includes determining the chemical composition of the object emitting the radiation, as well as other critical factors such as the presence of a magnetic field and its temperature. Optical luminosity, which corresponds to the optical part of the electromagnetic spectrum, holds particular interest due to our eyes' adaptability to observe the Universe within this range.

However, optical astronomy is not just limited to what we can see with our eyes; it has proven to be highly valuable and interesting when studying AGN for several reasons:

- AGN Spectral Features: Optical astronomy allows astronomers to capture the optical spectra of AGN. In the optical range, AGN emit a wide range of spectral features, including emission lines from ionized gases. These emission lines can reveal critical information about the physical properties of the AGN, such as their composition, temperature, density, and motion.

- Broadband Observations: The optical range provides broadband observations, enabling astronomers to collect data across a broad spectrum of wavelengths within the optical band. This is crucial for studying the entire energy distribution of AGN and understanding the complex interplay of various processes in their central regions.

- Host Galaxy Properties: Optical observations are not limited to the AGN itself but also encompass the light from the surrounding host galaxy. This is essential for studying the relationship between AGN activity and the properties of the host galaxy, such as its morphology, SFRs, and the influence of the AGN on its surroundings.

- Redshift Measurements: The optical spectrum of AGN often contains spectral lines that allow for precise measurement of their redshift. This is crucial for determining their distance and, consequently, their cosmic evolution and the large-scale structure of the Universe.

- Long-Term Monitoring: Optical astronomy is well-suited for long-term monitoring of AGN. Many AGN exhibit variability in the optical range over timescales from days to years, providing insights into their intrinsic processes and helping to constrain their physical properties.

One instrumental component central to spectroscopic investigations is the Robert Stobie Spectrograph (RSS). Designed for high-resolution imaging and long-slit spectroscopy, this advanced instrument plays a crucial role in the study of celestial objects. By employing the RSS, long-slit spectroscopy of the COSMOS field of the MIGHTEE survey [Jarvis et al., 2017] is conducted on a carefully selected subset of RQQs. These observations offer valuable insights into the properties and behavior of AGN, aiding our understanding of these fascinating cosmic entities. The extensive use of the RSS underscores its significance in facilitating cutting-edge research and driving our knowledge of the Universe to new frontiers.

### 1.1.3 Ancillary data

In addition to the optical data obtained by SALT, a complementary dataset comprising optical and NIR information from the Hyper Suprime Cam (HSC) and the VISTA Deep Extragalactic

Observations (VIDEO) survey will be utilized. VIDEO [Jarvis et al., 2013] is a 12 $\deg^2$, NIR five band (ZYJHKs) survey that is taken over the Elais-S1 ($\approx$ 3 square degrees), XMM-LSS ($\approx$ 4.5 square degrees) and the Extended Chandra Deep Field South (4.5 square degrees) tiles. As stated before, observations in the NIR are important due to their access to old stellar systems that are not necessarily visible in the optical. This is particularly important in having a non-biased age selection of star forming regions. Furthermore, FIR observations serve the purpose of excluding the influence of AGN contribution, allowing them to function as an autonomous indicator of the SFR.

## 1.2 Galaxies: What are they?

Galaxies can be thought of as being a collection of stars, dust, dark matter, and other mutual gravitationally bound cosmic bodies. A further grouping of these objects results in what is known as a galaxy cluster. For example, our Milky Way galaxy is part of the Virgo cluster, which also happens to be a part of a super cluster known as Laniakea. The hierarchical structure that these objects collectively form a part of is called the cosmic web and is composed of their filamentary aggregation along with areas of little to no baryonic content, known formally as voids (see Davies et al. [2021] for a discussion on cosmic void finders). The Universe has been proven to be periodic in the manner in which it clusters at different large redshifts [Namane et al., 2018]. Like many other cosmic objects, galaxies come in many forms, shapes and sizes. As a result, it is through studying these particular structures by means of tracing the distribution of neutral hydrogen, that one may be able to determine the mechanics associated with the dynamics of the Universe beyond galactic scales. Typically, galaxies span a range that starts from dwarf galaxies (see Thomas et al. [2006] for an exposition of VCC 510's kinematical and stellar population properties) to very large galaxies in terms of angular size [Roelfsema and Allen, 1985]. Within this domain lies all sorts of galactic morphological manifestations. However, there are formally four categories assigned to galaxy classes. These are:

1. Spiral galaxies
2. Elliptical galaxies
3. Barred galaxies
4. Irregular galaxies

The Jeans-Hubble tuning fork diagram is an illustration of what was thought to be the evolution sequence of galaxies. Astronomers have however since realised that blue spiral galaxies tend to

manifest their distinctive features during the earlier phases of cosmic evolution, often characterized by active SF, vibrant spiral arms, and ongoing morphological changes. On the other hand, elliptical galaxies typically come into existence through different processes and at different cosmic epochs. They often represent the end product of galactic evolution, arising from the merging of multiple spiral galaxies or through other mechanisms that lead to a spheroidal shape. The specific epochs and processes involved in the formation of elliptical galaxies vary, contributing to the nuanced cosmic timeline. Galaxy evolution is a complex process influenced by various factors. Tidal interactions, characterized by gravitational forces between galaxies, represent just one facet of this complexity. When galaxies gravitationally interact with one another, various effects unfold. The gravitational interaction can lead to the redistribution of gas within the galaxies. Some of the gas may remain bound to the system, while other portions could be stripped away or form tidal features. Additionally, the gravitational forces can induce distortions in the shapes of the interaction galaxies, altering their original structures. These changes in gas distribution and galactic morphology are significant outcomes of gravitational interactions between galaxies. Other processes contributing to galaxy evolution show that these diverse influences collectively shape the destiny of galaxies, highlighting the multifaceted nature of their evolutionary journey. In addition to tidal interactions, there are several other processes involved in the evolution of galaxies:

- ✓ Star Formation: The rate of SF within a galaxy can significantly impact its evolution. Galaxies that form stars at higher rates are often considered. "active", while those with lower SFRs are considered "quiescent". The balance between SF and the depletion of gas reservoirs is a critical aspect of galaxy evolution.

- ✓ Supernovae and Stellar Feedback: Supernova explosions and the feedback from massive stars can influence a galaxy's composition, structure, and energy balance. They inject energy and matter into the interstellar medium (ISM), affecting subsequent SF.

- ✓ Galactic Mergers: Mergers between galaxies can lead to significant changes in their structure and properties. During a merger, galaxies can lose their individual identities, and their structures may be altered. This process can trigger bursts of SF and the formation of new structures, such as elliptical galaxies.

- ✓ AGN: The presence of supermassive black holes (SMBHs) at the centers of some galaxies can lead to the formation of AGN. The energy released by AGN can affect the surrounding galaxy, influencing its SF and gas dynamics.

- ✓ Feedback from AGN: The activity of AGN can influence a galaxy's evolution by expelling gas, heating the ISM, and affecting the growth of BHs. This process is known as AGN

feedback and can regulate SF and BH growth.

- ✓ Cosmic Environment: The environment in which a galaxy resides, such as galaxy clusters or voids, can have a significant impact on its evolution. In dense cluster environments, galaxies may experience more frequent interactions and have their gas reservoirs stripped away, while galaxies in voids may evolve differently due to their isolation.

- ✓ Chemical Evolution: The enrichment of a galaxy's ISM with heavy elements (metals) through stellar nucleosynthesis and supernova explosions plays a role in its evolution. The metallicity of a galaxy affects its ability to form stars and the types of stars it can produce.

- ✓ Dark Matter: The distribution of dark matter within a galaxy can influence its dynamics and structure. Dark matter's gravitational pull can help stabilize galaxies against disruptive tidal forces and other perturbations.

- ✓ Galactic Winds: Galactic winds are outflows of gas from galaxies, driven by various processes such as supernovae and AGN activity. These winds can regulate the gas content of galaxies, affecting their ability to form stars.

- ✓ Hubble Sequence and Morphological Evolution: Galaxies follow a sequence from elliptical to spiral, based on their morphology. The evolution of a galaxy can involve transitions between these different morphological types.

- ✓ Cosmic Time and Redshift: The age of the Universe and the redshift of galaxies are essential factors in galaxy evolution. As the Universe expands, the properties and interactions of galaxies change over cosmic time.

Understanding galaxy evolution involves considering the interplay of these various processes and their relative importance in shaping the properties and characteristics of galaxies in the Universe.

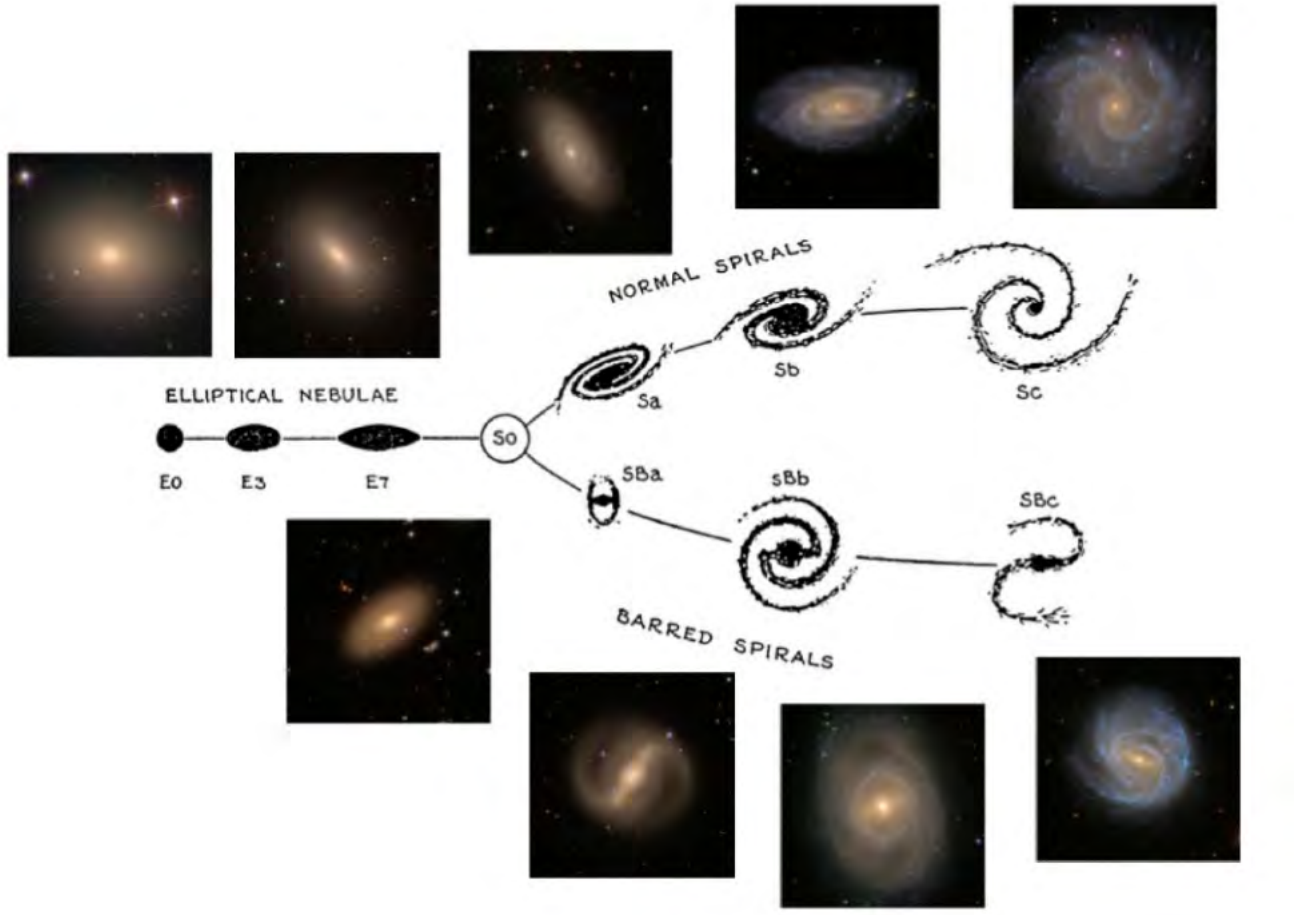


**Figure 2:** Jeans-Hubble tuning fork. Image extracted from the work of Hubble [1936].

### 1.2.1 Star Forming Galaxies (SFGs)

In order to understand what SFGs are, one first needs to comprehend what stars are and the role that they play in demarcating a clear distinction between star forming and quiescent galaxies. Stars form as a result of the gravitational collapse of molecular clouds that subsequently initiate the nuclear fusion reactions that give rise to the creation of elements during their lifetime. These molecular clouds form as a result of the accumulation of dust and gas. Some of these galaxies then undergo numerous gravitational interactions with other cosmic bodies. SFGs, constitute one of the primary categories of galaxies in the study. They are distinguished from other categories, such as quiescent galaxies, which have ceased or significantly reduced their SF activity, and AGN galaxies, which harbor an active central SMBH. Among SFGs, those that exhibit a reduction in their SFR are referred to as quenched, as previously mentioned. The mechanism that quenches the SF is believed to be connected to the AGN, e.g. the radio jets, which have since switched off.

This distinction helps to clarify that not all galaxies are considered SFGs and emphasizes that the term quenched is applied within the context of this specific galaxy classification. It is currently believed that the growth rate tied to the population of quenched galaxies with moderate to low velocity dispersions can be correlated to a decrease in SFGs with similar dispersions [Bezanson et al., 2012].

### 1.2.2 Active Galactic Nuclei (AGN)

AGN are comprised of a SMBH that is actively accreting material acquired from its host galaxy or the circumgalactic medium and radio jets that sometimes form as a result of this. Over the years, radio loudness in the context of AGN has been a subject of ongoing investigation, leading to different definitions proposed by various researchers. Kellermann et al. [1989] put forth one of the initial definitions, considering radio loudness as the ratio of the radio luminosity to the optical luminosity of an AGN. This definition aimed to distinguish between AGN exhibiting strong radio emission and those with relatively weaker radio emission. However, Kellermann et al. [2016] later challenged their previous definition, recognizing that the relevant measure of radio loudness is neither the radio flux density nor the radio-optical flux density ratio. Rather, it is the radio luminosity that is better suited to determine radio loudness.

Another significant contribution to the understanding of radio loudness came from Padovani et al. [2009]. They extended the concept by introducing a classification scheme based on the AGN's radio spectral energy distribution (SED) in comparison to its optical SED. Padovani et al. [2009] classified AGN as either radio loud or radio quiet, depending on the relative dominance of radio emission in their SED.

To illustrate their findings, Padovani et al. [2009] presented Figure 3 in their paper, which depicted the radio to optical flux ratio for a sample of AGN. This figure visually demonstrated the separation between radio loud and radio quiet AGN based on their spectral properties.

The revisions introduced by Kellermann et al. [2016] and the classification scheme proposed by Padovani et al. [2009] exemplify the ongoing efforts to refine and redefine our comprehension of radio loudness in the fascinating realm of AGN. These distinct definitions highlight the dynamic nature of the field and the intricate interplay between the radio and optical properties of AGN. As researchers continue to explore the complexities of radio emissions in AGN, these advancements contribute to our evolving understanding of these enigmatic cosmic entities.

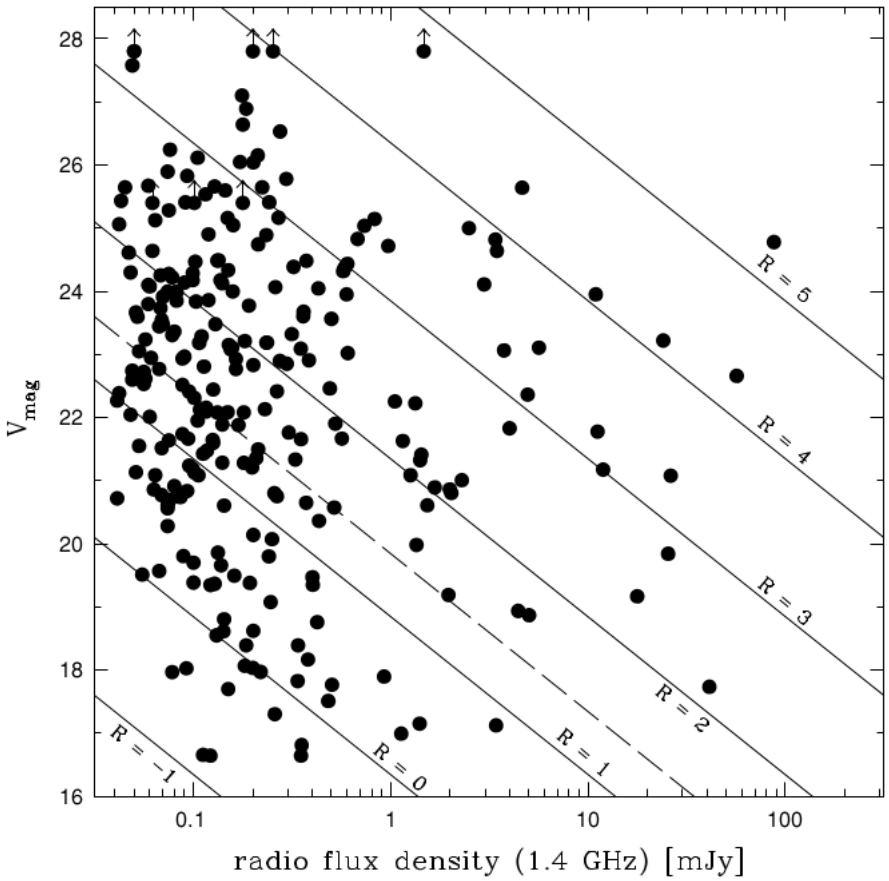


**Figure 3:** Plot showing the relationship between V-band magnitude and 1.4 GHz radio flux density for the selected sample. Arrows represent lower limits of V magnitude, while lines indicate different values of the radio to optical flux density ratio [Padovani et al., 2009]. This ranges from $R = 5$ (radio loud) to $R = -1$ (radio quiet), and the separation between the two distinct populations of AGN is represented by the dashed diagonal line.

The study of radio galaxies and the feedback from AGN jets, as extensively reviewed by Hardcastle and Croston [2020] in their work, provides valuable insights into the understanding of radio loud quasars (RLQs). RLQs, which have garnered significant attention in the field of astrophysics, are known for their intense radio emission originating from the central region of the galaxy. They are composed of a central BH and an accretion disc surrounding it, which plays a pivotal role in the formation of the powerful jets observed in RLQs.

In a recent investigation by Dogruel et al. [2020], X-ray data were utilized to monitor a specific selection of three gravitationally lensed RLQs. These gravitationally lensed RLQs exhibit distinct characteristics, consisting of a central BH and a surrounding accretion disc. The formation of the jet in these objects is hypothesized to be influenced by the mass of the BH and other

physical characteristics associated with the accreting medium. The study provides insights into the X-ray emission characteristics of gravitationally lensed RLQs, highlighting differences in the detected features and sizes compared to RQQs. It concludes that RLQs exhibit larger unresolved X-ray emission sizes compared to RQQs, suggesting a more prominent contribution from jets, as indicated by Bayesian analysis.

These objects also sometimes come in strange morphologies such as in the case of PKS2014-55, whose X-shaped radio emission is suggested to be as a result of hydrodynamical backflow [Cotton et al., 2020]. Figure 4 is a 1.28 GHz MeerKAT image of PKS2015-55, which is a 2.36 Jy radio source and has a spectral luminosity of $2 \times 10^{25} \mathrm{WH}z^{-1}$. On the other hand, RQQs are a subclass of quasars that exhibit much weaker or undetectable radio emission compared to their radio loud counterparts. Unlike RLQs that display intense radio emission originating from the central region of the galaxy, RQQs have significantly lower levels of radio activity. The main distinction between RQQs and RLQs lies in the strength of their radio emission, which is believed to arise from different physical mechanisms. While RLQs are powered by the interaction between the central SMBH and the accretion disc, it is still yet to be determined if RQQs are characterized by a less prominent accretion process. This difference in radio activity suggests that RQQs may have lower levels of jet formation or less energetic jet outflows compared to RLQs. Additionally, the study of RQQs provides insights into the role of accretion processes and the interplay between the central BH and the surrounding medium in shaping the observed characteristics of quasars.

## 1.3 Black holes (BHs)

A BH is a region in space with intense gravity where nothing, including light, can escape. Formed from the remnants of massive stars undergoing gravitational collapse, a BH's event horizon marks the point of no return, beyond which the laws of physics break down and space-time curvature becomes infinite. BHs vary in size and mass, ranging from a few solar masses to millions or billions. They are highly dense and exert strong gravitational forces. These objects are subjects of extensive study in astrophysics and cosmology.

### 1.3.1 Supermassive (SM) vs stellar-mass BHs

SMBHs are found at the center of their host galaxies. Due to their presence, these SMBHs are responsible for the jets that are observed to play a role in the evolution of quasars. The work by Bromm and Loeb [2003] suggests a scenario in which specific conditions in early metal-free galaxies contribute to the formation of SMBHs, including binary systems, with potential implications for

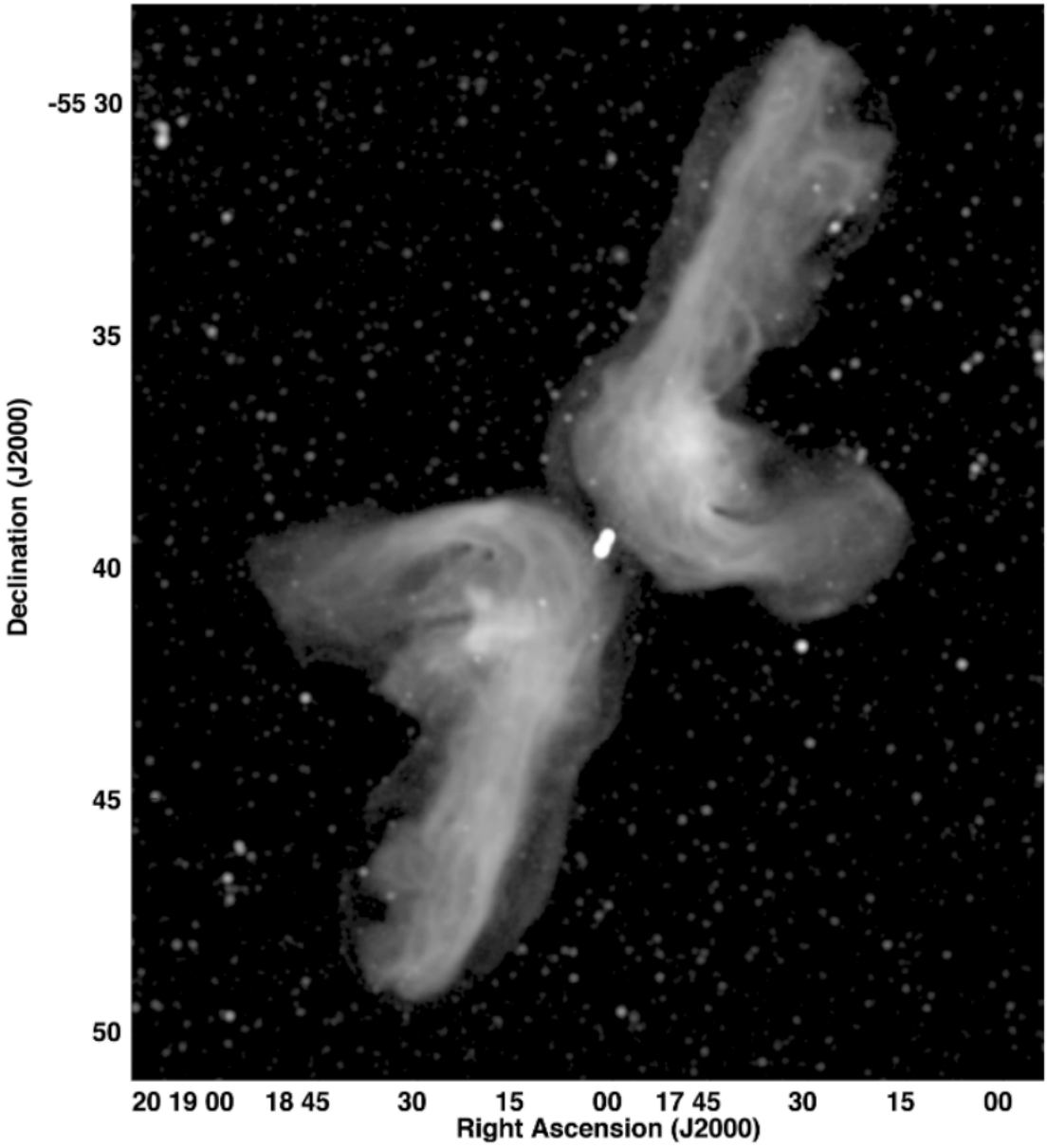


**Figure 4:** X-shaped AGN example [Cotton et al., 2020].

quasar activity and gravitational wave detection. They typically exhibit masses within the range of $10^6$ to $10^{10}$ times that of the Sun ($M_\odot$). This phenomenon is observed in the nuclei of most, if not all, nearby galaxies, emphasizing the widespread presence of SMBHs in the cosmic landscape [Simon, 2023]. Stellar-mass BHs on the other hand are one of two potential end products of a star's life cycle. As stated in Section 1.2.1, stars can be thought of as being nuclear reaction regions that are a direct consequence of gas, dust and gravity. Ultimately, stars that are significantly hotter

($5500°C$) and larger ($1.392 \times 10^6$ km in diameter) than the mass ($1M_\odot = 1.99 \times 10^{30}$ kg) of our Sun exhaust their fuel, and in the end, gravity prevails over the ongoing nuclear fusion processes, leading to an explosive event known as a supernova. Stars surpassing the Chandrasekhar limit, approximately $1.4M_\odot$, are anticipated to undergo gravitational collapse, resulting in a transformation into diverse stellar remnants, such as neutron stars or BHs.

Fryer and Hungerford [2005] acknowledge that the details of the supernova mechanism are not completely understood, but suggest that the modeling of stellar collapse provides intuition about the qualitative features of neutron SF. The review explores formation process scenarios and discusses how our understanding of these processes can be applied to constrain aspects such as neutron star kick mechanisms, supernova asymmetries, and the relationship between stellar rotation and neutron star magnetic fields. It also touches upon the constraints imposed by observed populations of pulsars and magnetars. When a white dwarf's mass exceeds the Chandrasekhar limit, the electron degeneracy pressure within its core becomes inadequate to counterbalance the gravitational self-attraction, initiating gravitational collapse. Consequently, white dwarfs with masses surpassing the Chandrasekhar limit are anticipated to evolve into BHs. This limit serves as a crucial threshold for stability. White dwarfs with masses up to the limit typically maintain stability, while those exceeding it are predisposed to collapse into more compact configurations, including the formation of BHs. Therefore, stars that are expected to become BHs are those white dwarfs with masses exceeding the Chandrasekhar limit. This limit acts as a critical threshold for stability.

### 1.3.2 Primordial BHs

Today, there are many theories that seek to explain the origin of the Universe through the use of an all encompassing equation that is capable of describing everything. Mainstream cosmology currently leans on the origin of the Universe being due to inflation [Guth, 1998], and it has since been the hope of numerous theorists to formulate a theory of gravity that explains the Big Bang as well as the current accelerated expansion of the Universe that is thought to be as a result of what is known as dark energy (see Sami et al. [2018] for the use of a modified form of gravity that negates the need for the usage of an unknown dark sector). In line with this, primordial BHs are thought to be BHs that existed in the early Universe. Some people have even pointed to the potential that these objects have in explaining what dark matter could be [Carr et al., 2016].

## 1.4 AGN feedback

Both the ISM and intergalactic medium (IGM) are critical components in the study of galaxy evolution as they strongly influence the dynamics and processes taking place within galaxies. AGN are powerful energy sources located at the centers of galaxies, fueled by the accretion of matter onto a SMBH. AGN feedback refers to the reciprocal interaction between the AGN and its surrounding gas and environments, where the energy and radiation released by the AGN have significant effects on the surrounding gas and can impact the growth and evolution of the galaxy hosting the AGN.

Figure 5 provides insights into the observation of AGN from different angles of incidence, highlighting the orientation effects that can influence our perception of AGN properties. Understanding these effects is crucial in accurately interpreting AGN observations and studying their impact on galaxy evolution. The figure also draws attention to a relationship within AGN, specifically between the flux emitted by the accretion disk, which is responsible for emitting the intense radiation, or flux, observed in AGN, and the torus, which plays a role in blocking and shaping the observed radiation, affecting the appearance of the AGN in different wavelengths and observational classifications. The torus doesn't emit the primary flux, but can influence how we perceive and classify AGN based on our line of sight and the wavelength of the resulting radiation. At larger radii, more emission occurs at different wavelengths, implying that as you move outward from the central SMBH, the radiation emitted varies in wavelength. This variation is intricately linked to the dynamic interplay of processes such as accretion, outflows, and the distribution of matter. The SED of an AGN should be meticulously analyzed to understand how these dynamics, including changes in temperature, density, and composition of the accretion disk and outflows, influence the emitted radiation. Here's how SEDs are relevant to AGN:

- Diagnostic Tool: AGN SEDs serve as diagnostic tools to categorize and understand the nature of the energy sources within these galaxies. They provide insights into the physical conditions and processes near the SMBH, as well as the surrounding regions.

- Accretion Disk: The high-energy, short-wavelength portion of the SED is often dominated by X-ray and ultraviolet (UV) emission, which originates from the accretion disk surrounding the SMBH. Analyzing this part of the SED helps astronomers understand the accretion rate and temperature of the disk, shedding light on BH feeding and growth.

- Broad Line Region (BLR): Emission lines in the UV and optical wavelengths stem from the BLR, which is a region of ionized gas surrounding the central BH. These lines provide information about the gas dynamics and the BH's mass.

- Narrow Line Region (NLR): For sources that are at low redshift, emission lines in the optical and NIR regions are associated with the NLR, which contains lower-density, more distant gas. NLR lines offer insights into the overall energetics of the AGN and its impact on the host galaxy. These lines, emitted by ionized gas in the region surrounding the central supermassive BH, give clues of the AGN's energy output. By analyzing the intensities and ratios of NLR lines, astronomers can estimate key parameters such as gas density, temperature, and chemical composition, providing a comprehensive understanding of the AGN's radiation emission. Moreover, the study of NLR lines aids in assessing the influence of the AGN on the host galaxy. Processes associated with AGN, such as radiation pressure and powerful outflows, affect the surrounding gas and star-forming regions. Observations of NLR lines contribute to elucidating how AGN feedback mechanisms regulate SF and impact the broader evolution of the host galaxy. However, BLRs are much closer to their respective SMBH than NLRs are.

- Dust Torus and IR Emission: The SED may exhibit a significant IR component originating from a dusty torus that surrounds the AGN. This dust can absorb and re-radiate energy, and its SED component provides information about the geometry and orientation of the torus.

- Variability and Evolution: SEDs can change over time due to variations in accretion rate, BH activity, and the complex interplay of matter in the AGN environment. Monitoring AGN SEDs can reveal information about the dynamics and evolution of these active galaxies.

- Classification: Different types of AGN, such as quasars and Seyfert galaxies, can be distinguished based on their characteristic SEDs. For example, quasars are known for their exceptionally high luminosity and exhibit specific SED features such as a power-law continuum, UV emission lines and non thermal high energy output, while Seyfert galaxies have SEDs consistent with lower luminosities.

AGN feedback is a fundamental mechanism that can shape the properties of galaxies. The energy and radiation released by the AGN can heat or drive out gas from the host galaxy, affecting the SFR, gas distribution, and overall morphology of the galaxy. This feedback process plays a significant role in regulating the growth of galaxies and influencing their evolutionary paths. Understanding AGN feedback is crucial in comprehending the intricate interplay between SMBHs, their host galaxies, and the surrounding gas, shedding light on the complex mechanisms that drive galaxy evolution. A radio survey key to observing this, known as the MIGHTEE survey, is discussed in subsequent chapters.

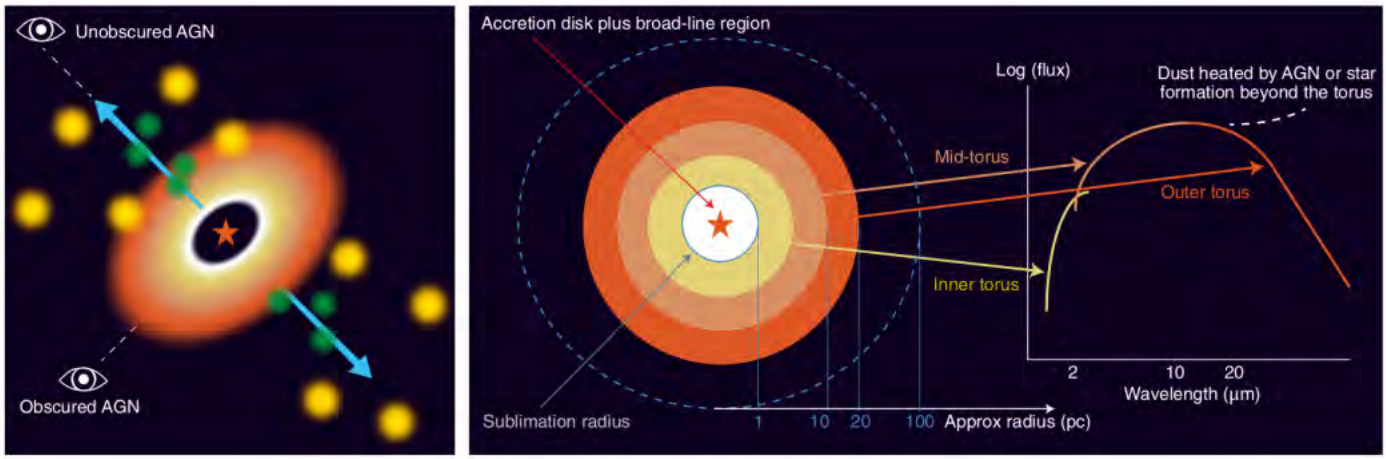


**Figure 5:** A typical AGN along with its surrounding torus. The star in the image represents the region where a BH is thought to reside [Lacy and Sajina, 2020].

## 1.5 AGN vs SF

SF and AGN activity form an integral role in galaxy evolution studies. From observations of different sections of the electromagnetic spectrum, it is possible to deduce that both of these processes populate a huge share of emission observed at different frequency bands. When it comes to SF, radio emissions are not directly associated with the supernovae explosions themselves. Instead, they stem from the supernova remnants, which are the aftermath of these explosive events. In addition to supernovae, HII regions also contribute to the observed radio emission through free-free emission [Kimball et al., 2011]. AGN on the other hand, exhibit radio emissions not only from the radio plumes and accretion discs observed as a result of potential feedback activity among the radiatively efficient SMBHs found in quasars, but also from the accretion disc itself. Using the MeerKAT International GHz Tiered Extragalactic Exploration (MIGHTEE) survey, an attempt at directly identifying RQQs found within the COSMOS field is made and in so doing, we continue in the trajectory of many studies tied to the investigation of AGN-related in contrast to SF-related radio emission, especially where RQQs are concerned. Owing to the fact that RLQs form about less than ten percent of the total quasar population [Kukula et al., 1998, Panessa et al., 2019], the issue of stellar dominance amongst radio emission at low luminosities is a scenario that requires further investigation. This is substantiated in work such as that of White et al. [2017], wherein a fixed redshift range of RQQ targets was utilized and it was found that it is quasar activity that gave rise to the majority of radio emission detected from the optically selected sample used in the study.

## 1.6 Outline of thesis

This thesis is structured as follows:

Chapter 1 is the introduction, wherein a brief overview of the objects of interest is made. A brief description of the mechanisms used to observe these targets is also discussed. The next chapter goes over the multi-wavelength scheme used for the analysis of the datasets used in this study. Chapter 3 deals with attaining the spectroscopic redshifts of sources by means of the Southern African Large Telescope. This is done namely through the use of the RSSMOSPipeline. The fourth chapter is an introduction to the concept of radio interferometry. It also covers the radio data used in this study and how it was obtained. Finally, chapter 5 goes over concluding remarks and possible future work.

# 2 Optical/NIR selected RQQs of the MIGHTEE survey

"From a small seed, a mighty trunk may grow"

Aeschylus

To further investigate the dichotomy that exists between SF and AGN activity within the context of radio emission, we select a sample using optical/NIR data and study the SFR template fittings within the sample selection. SFR template fittings involve comparing observed data to a library of templates representing different SF scenarios to estimate the rate at which stars are forming in a given system. This is done, so as to acquire an accurate mapping of the ratio between the radio SFR vs the optical/NIR SFR. At faint radio emissions however, disentangling radio emission tied to stars vs AGN activity is a difficult task. Firstly, the mechanism by which RQQs produce their radio emission is still a topic of discussion. As a result, it is very easy to mistake star forming regions for accretion activity. Secondly, tracking the evolution of galaxies in terms of parameters such as redshift and stellar mass, see Delvecchio et al. [2021], can be limited by a whole range of factors such as Malmquist bias, which is an effect that gives rise to the preferential detection of bright sources, for example. Be that as it may, there are still ways in which an attempt at differentiating SF from accretion may be adequately pursued.

For example, RLQs can be distinguished from star forming regions based on their distinct X-ray emission patterns, as described by the BH fundamental plane relation [Merloni et al., 2003]. The fundamental plane within this context is a relationship observed in astrophysics that connects the mass of a SMBH at the center of a galaxy, the mass of the galaxy's bulge (the central, dense part of the galaxy), and the stellar velocity dispersion in the bulge. Extending this concept to include the parameters of the Fundamental Plane for RLQ-BH mass, (5-GHz) radio continuum luminosity, and (2-10 keV) X-ray luminosity, a more intricate relationship emerges. The BH mass reflects the gravitational influence at the galactic core, while the (5-GHz) radio continuum luminosity signifies the quasar's radio emission. This emission is influenced by accretion processes and jet activities associated with the SMBH. Additionally, the (2-10 keV) X-ray luminosity provides insights into the quasar's high-energy processes. The interplay between these parameters in the Fundamental Plane offers a comprehensive perspective on the complex dynamics of RLQs.

This relation helps scientists understand the interplay between SMBHs and the properties of their host galaxies. In essence, it provides insights into how the growth of SMBHs is linked to the evolution of the galaxies they reside in. This relation is closely associated with the torus surrounding RLQs, which plays a significant role in shaping their observable characteristics. The

torus, consisting of dense gas and dust enveloping the central BH, influences the X-ray emission properties, contributing to the differentiation of RLQs from other sources. Although the three dimensions of the fundamental plane relation do not directly pertain to the torus itself, they capture the intricate interplay among the BH mass, accretion rate, and X-ray luminosity, thereby offering valuable insights into the nature of RLQs.

In addition to the fundamental plane relation, the investigation of the point-like nature of faint radio sources can serve as another useful tool. This can be accomplished by implementing a morphology cut, utilizing a different parameter derived from the K-band image, such as the K CLASS STAR. Such an analysis aids in discerning the underlying structure and nature of the faint radio sample, providing complementary information to further characterize these sources.

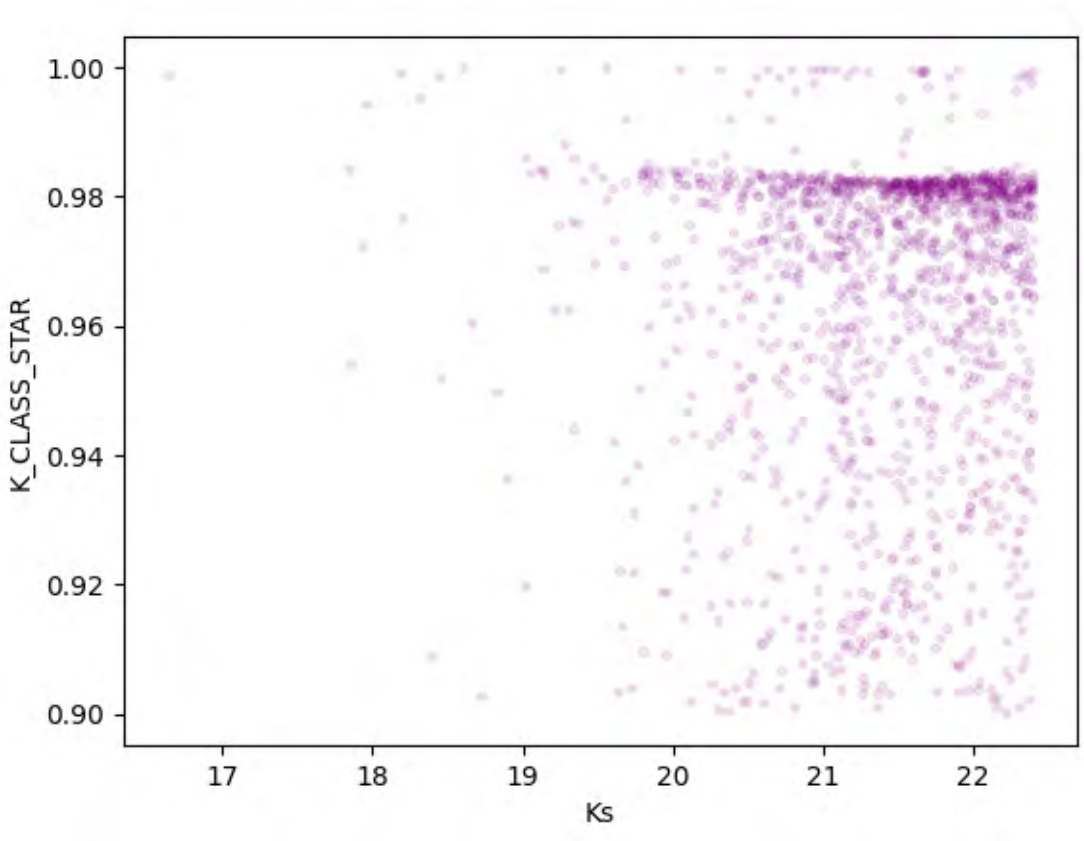


**Figure 6:** K CLASS STAR variation as a function of Ks band image for the selected objects. Objects with K CLASS STAR values above 0.9, indicating a degree of compactness, are included in the study.

White et al. [2015] point out that correctly classified simulated AGN, that have point-like characteristics must possess a K CLASS STAR value of close to 1, i.e. K CLASS STAR $> 0.9$. The K CLASS STAR value refers to the spectral classification of a star, indicating its temperature and characteristics within the K spectral type range. In Maddox et al. [2008], it is shown that a well defined sample of quasars presents itself at a $K_s$ band given by $17 \leq K_s \leq 22.4$. Figure 6 shows an agreement to this due to the majority of sources that converge onto 1 lying in the range $19.5 \leq K_s \leq 22.4$. A small portion of our sample is a part of type 1 quasars found within the black-boxed demarcation in the optical/NIR colour-colour plot shown in Figure 7. This colour-colour plot is the second step towards separating AGN candidates from stars. The following are equations that have been adapted from White et al. [2015] and describe the box region that had been mentioned.

$$J - K = -0.30 \tag{1}$$

$$g - J = -1.00 \qquad -0.30 < J - K < 1.10 \tag{2}$$

$$g - J = 0.65 \qquad -0.30 < J - K < 1.10 \tag{3}$$

$$J - K = 1.10 \tag{4}$$

In Figure 7, the equations derived to describe the grey lines alongside the quasar track are described as follows:

1. Line 1: $x_1$, $y_1 = [-0.30, 0.15], [-0.30, 5.0]$
   Equation: $y = 18x - 0.3$
   Slope: $m = 18$
   Y-intercept: $c = -0.3$

2. Line 2: $x_2$, $y_2 = [0.15, 0.2], [5.0, 7.5]$
   Equation: $y = 25x + 1.125$
   Slope: $m = 25$
   Y-intercept: $c = 1.125$

3. Line 3: $x_3$, $y_3 = [0.2, 0.18], [7.5, 10]$
   Equation: $y = 62.5x + 3.75$
   Slope: $m = 62.5$
   Y-intercept: $c = 3.75$

4. Line 4: $x_4$, $y_4 = [0.18, 0.14], [10, 12.5]$
   Equation: $y = 125x + 17.5$

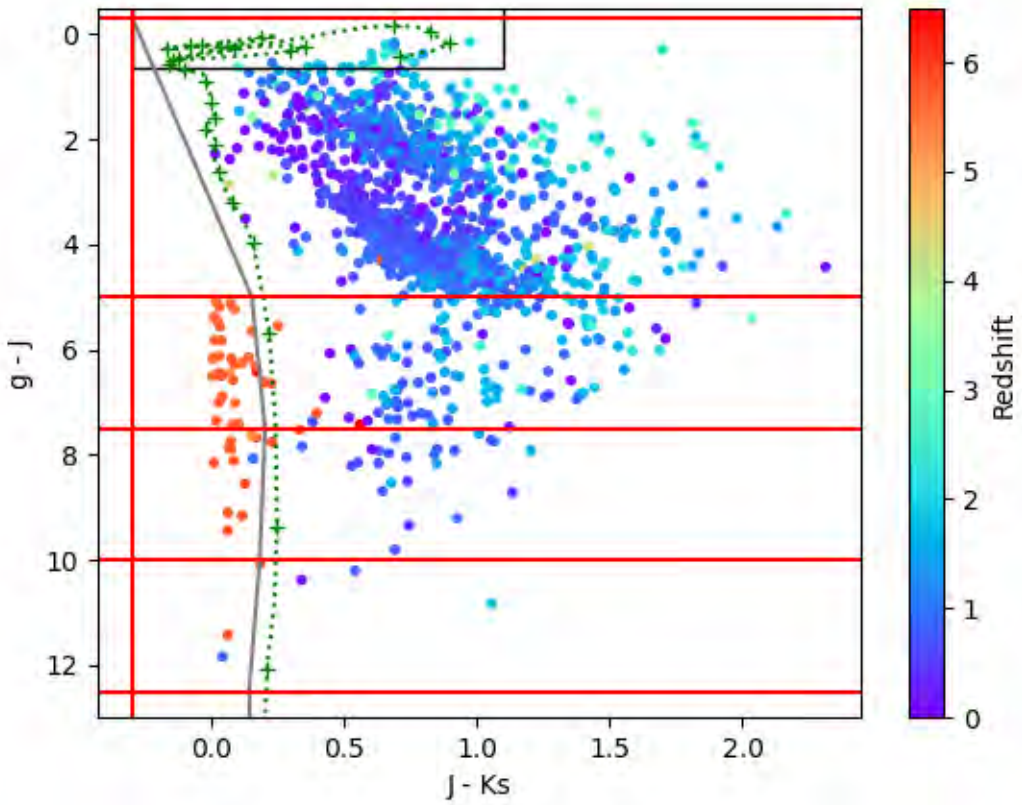


**Figure 7:** A colour-colour magnitude plot of AGN selected via an optical/NIR scheme. The AGN candidates are represented by data points, and a specific region highlighted by a black-box indicates AGN identified as quasar candidates. To aid in the classification process, a quasar track (green dotted line with crosses that represent redshift steps) adapted from White et al. [2015] is included, along with a grey line that serves as a boundary between stellar sources on the left and 1384 AGN candidates on the right, leaving 42 sources that are believed to be stellar. The equations for the grey line can be found on the following page. Additionally, red lines are incorporated to facilitate the counting of the AGN population.

Slope: $m = 125$
Y-intercept: $c = 17.5$

5. Line 5: $x_5$, $y_5 = [0.14, 0.14], [12.5, 17.5]$
   Equation: $x = 0.14$
   A vertical line is defined by a constant value of $x$ and does not have a slope-intercept form.

The equations are now correctly represented in slope-intercept form ($y = mx + c$), where "$m$" represents the slope and "$c$" represents the y-intercept.

## 2.1 Photometric template fitting

In the research conducted by Adams et al. [2020], a crucial initial step in the analysis of each passband was to acquire their photometric properties. This essential task was accomplished through the utilization of a sophisticated software known as LePhare, developed by Stephane Arnouts and Olivier Ilbert [Arnouts and Ilbert, 2011]. LePhare enabled the fitting of hundreds to thousands of photometric templates to the observed data, allowing for a comprehensive exploration of the photometric properties of each passband. By employing this approach, the selection criteria employed for the detection of the objects of interest, which in this case were quasars, underwent further refinement and optimization.

The process of fitting photometric templates using LePhare, which includes three sets of libraries for galaxy SEDs, stellar SEDs, and AGN SEDs, played a vital role in refining the characterization and identification of quasars. The software functioned by minimizing the chi-square ($\chi^2$) value of galaxy and stellar SED templates, fitting them to the multi-band photometry, and accounting for uncertainties. Subsequently, the optical/NIR SFRs were then outputted by the LePhare fitting. To facilitate this fitting process, the uncertainties of the photometry were set to a minimum of 5 percent. LePhare, utilizing its diverse SED libraries, was run on all sources identified by SExtractor over an extensive imaging area of approximately 6 square degrees.

$\chi^2$ minimization is a fundamental statistical technique used in the fitting of photometric templates to observed data. In Adams et al. [2020], the process of $\chi^2$ minimization played a crucial role in determining the best fit parameters for the galaxy SED templates. The concept of $\chi^2$ involves comparing observed data with model predictions to quantify their agreement. The $\chi^2$ statistic is calculated by taking the squared difference between the observed data and the corresponding model predictions, weighted by the uncertainties associated with the measurements. By summing up these squared differences across all data points, the $\chi^2$ value is obtained. The goal

of $\chi^2$ minimization is to find the set of model parameters that minimizes the overall $\chi^2$ value, indicating the best fit to the observed data. The following is a representation of this technique, where $(O_i)$ and $(E_i)$ are the observed and expected value of the $i$th data point, respectively.

$$\chi^2 = \sum_i \frac{(O_i - E_i)^2}{E_i} \tag{5}$$

In the case of the photometric template fitting performed using LePhare, minimization was employed to adjust the parameters of the galaxy SED templates. This adjustment aimed to achieve the closest match to the multi-band photometry. The uncertainties of the photometry were considered during the minimization process to ensure accurate estimation of the goodness of fit. By finding the set of parameters that yields the minimum $\chi^2$ value, the best fit SED templates were identified, providing insights into the photometric properties of the objects under investigation, such as quasars.

## 2.2 Sample selection

The sample used in this study combines optical data acquired from the Canada-France-Hawaii Telescope and NIR data from the VISTA Deep Extragalactic Observations (VIDEO) survey, as provided by Adams et al. [2020]. The data in the samples were initially represented as fluxes and needed to be converted to absolute magnitudes. Specifically, the conversion was performed in the AB system, which is commonly used in astronomy.

To convert the flux in the J band to the absolute magnitude of J, the following equation was applied:

$$|J| = -2.5 \log_{10}(\Phi_J) - 48.60 \tag{6}$$

In this equation, $\Phi_J$ represents the flux in the J band. By taking the logarithm of the flux and applying a scaling factor, the equation calculates the absolute magnitude of J. This conversion allows for a standardized representation of the magnitude in the AB system, providing a consistent framework for comparing and analyzing astronomical observations.

Magnitudes are measured using two main systems: the Vega system and the AB system. In the Vega system, the apparent magnitude of the star Vega serves as the zero point in each passband. This choice of Vega as a reference is crucial for calibrating magnitudes in various filters, providing a baseline for astronomical observations. On the other hand, the AB system establishes its scale based on a constant flux density across all passbands, offering a different approach to

magnitude calibration.

## 2.3 *gJKs* colour-colour selection

The AGN selection scheme known as *gJKs* has been proven to be effective in studies aimed at differentiating AGN from stars, as demonstrated in work such as that of Maddox et al. [2008] and White et al. [2015]. In Figure 8, the spectra and filter response curves for the g, J, and K bands are

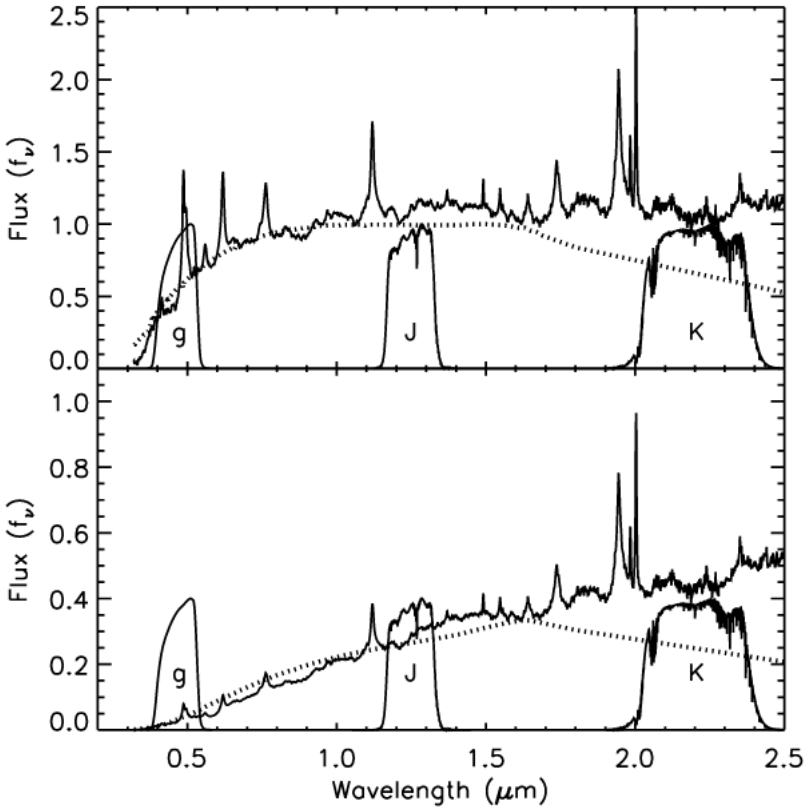


**Figure 8:** Figure showcasing a detailed comparison of the SEDs between a quasar and a stellar source. The SEDs are depicted for different wavelength bands, namely g, J, and K. In the top and bottom part, a quasar spectrum represented by the solid line at redshift z = 3 is shown. The early K-star spectrum shown by the dotted line in the top plot reveals a notable K-band excess in quasars. In the bottom part, when extinction is considered, the K-band moderation in an early M-star (dotted line) remains prominent. The reason the K-band excess is considered is that it provides a reliable means of distinguishing between quasar and star SEDs. It highlights the significant difference in flux gradient between quasars and stars within the K-band filter, even when considering extinction. This emphasizes the challenge of accurately discerning between quasar and star SEDs in the presence of extinction [Maddox et al., 2008].

presented. This visual representation enables a detailed examination of the SEDs of a stellar source and a quasar. By analyzing the figure, it becomes evident that a clear separation exists between

the SED characteristics of the stellar source and the quasar. This distinction is manifested in the different shapes and intensities of the SED curves across the three bands. In particular, there is a notable discrepancy in the K band, indicating a significant difference in the flux measurements between the two sources. As a result, a cut in the $K_s$ value can effectively be employed as a criterion for distinguishing between stellar sources and quasars. The observed distinct separation in the SEDs further supports the utility of the *gJKs* selection scheme in accurately classifying and identifying these two types of astronomical objects. In order to get the colour magnitude plot shown in Figure 7, one first has to go through a series of steps that are listed below.

- A FITS file containing parameters such as the right ascension and declination of the optical/NIR sample was opened.
- In the process, template fitting was conducted, and the $\chi^2$ values used in the subsequent analysis were derived from this template fitting procedure discussed in an earlier subsection (see Section 2.1). The $\chi^2$ values were then utilized to filter the sources based on their respective $\chi^2$ values, indicating the quality of fit with different templates. Specifically, the $\chi^2$ values were compared to ensure that $\chi^2_{QSO} < \chi^2_{Gal}$ and $\chi^2_{QSO} < \chi^2_{Star}$, where the subscripts QSO, Gal, and Star represent the quasar, galaxy, and stellar components, respectively. These selection criteria were applied to prioritize the identification of quasars by favoring data points that exhibit the best fit with a quasar/AGN model rather than a star or galaxy model. This approach underscores the significance of template fitting and the use of $\chi^2$ values in discerning and characterizing quasars within the scope of this study.
- Finally, the sources were selected according to their absolute $K_s$ magnitude. White et al. [2015] impose a cut of $K_s \leq 22.4$ in order to ensure that the NIR morphology of the candidate AGN is reliable.

The green dotted and grey lines in Figure 7 are somewhat of a demarcation between stellar sources found on the left and AGN point sources found on the right. On the other hand, objects whose quasar status is more reliable are clearly demarcated. Among the data points fitted with AGN templates, there exists a varying degree of separation from the galaxy cluster. While some data points show distinct separation, others exhibit more significant overlap with the galaxy region. The black-box region is where a large portion of the quasar track (green dotted line) resides, and so this region of *gJKs* space offers the best chance of reliably identifying quasars. The total number of points on the *gJKs* plot is 1426. Using these points justifies the differentiation between stellar, galaxy and AGN sources and a count of the number of AGN candidates is made, which accounts to 1384 AGN candidates. The colour bar shown on the right of the colour-colour plot is the photometric redshift scale of the targets identified, and it is safe to say that the objects on the

left do not conform to the quasar template used for the analysis due to the high average redshift observed.

# 3 SALT spectroscopic redshifts

"Woza uzobabona"

Pro, *Wozobona*

Despite initially identifying 1384 AGN candidates, it is crucial to note that out of those, only ten COSMOS quasars are under investigation, as depicted by the black-boxed region in Figure 7. This chapter goes over the procedure used to attain the spectroscopic redshifts of the said targets. Each quasar is run through a pipeline that is meant to separate them from other spectral sources. In addition to locating the targets of interest, the pipeline is tasked with ultimately providing spectra of the sources. Before this however, data is taken in from SALT's pipeline folder, containing preprocessed optical/NIR data tied to the intended targets. This is then passed over to the RSSMOSPipeline. Details of this preprocessing is presented in the succeeding section.

## 3.1 Using SALT

The SALT primary reduction pipeline is a data processing system designed to handle the initial stages of reducing raw data obtained from the telescope's instruments. The primary reduction pipeline is crucial for converting raw observational data into scientifically useful data by applying various corrections and calibrations. Using this, the SALT observations underwent several processing steps to prepare the data for analysis before being fed into the RSSMOSPipeline (see Section 3.3). The steps included in the data reduction pipeline are described as follows:

1. Fidelity checking: The integrity and quality of the data were assessed to ensure that it was suitable for further processing.This involves bias plus dark current correction, trimming and masking, wavelength calibration, and alignment coupled with stacking.

2. Flat-fielding: Spectroscopic lamp flats were utilized to correct for variations in pixel-to-pixel sensitivity and distortions in the optical path. The flat images were normalized using the median value to transfer multiplicative errors without significantly altering the pixel values.

3. Gain correction: The pixel values were corrected for the gain of the detector to account for any systematic variations in the signal response.

4. Cosmic ray rejection: To eliminate artifacts caused by cosmic rays, three exposures were taken for each target with different exposure times. A comparison was made between the pixel values in the three images, and unusually high values above a sigma threshold were removed. Additionally, the distinct appearance of cosmic rays as bright spots or streaks facilitated their identification and removal.

5. Cross-talk correction: Corrections were applied to mitigate any interference or contamination between adjacent detector pixels.

6. Wavelength calibration: The spectra were calibrated for accurate wavelength determination by using an argon lamp to illuminate the grating. The resulting emission lines, affected by the grating's angle, were corrected for distortion. Cropping of the 2D images in the slit direction was performed to address difficulties encountered in fitting a polynomial to the large curvature of the emission lines.

7. Bias subtraction: The bias level, resulting from electronic noise in the detector, was subtracted from the images.

8. Background subtraction: The contribution of the sky background was removed by fitting a polynomial to regions adjacent to the target along the slit dimension. This fit was then extrapolated over the target area and subtracted from the total flux spectrum. The removal of sky emission lines originating from atmospheric elements, such as oxygen, was an additional benefit of this process.

9. Amplifier mosaicing: If multiple amplifiers were used during the observations, the individual amplifier images were combined into a single mosaic image.

By following these steps, the data was corrected for various instrumental and atmospheric effects. This also made the data suitable for subsequent analysis and interpretation.

## 3.2 Wavelength Calibration

Wavelength calibration is a necessary step in adequately doing astronomical spectroscopy, this leads to an accuracy of the observed spectral data. It involves aligning the recorded wavelengths of spectral features with their true values. This calibration corrects for instrumental effects, such as grating imperfections and thermal variations, which can introduce errors in the measured wavelengths. Precise wavelength calibration is essential for extracting reliable physical information from spectra, such as redshift measurements for distant celestial objects. The calibration process typically utilizes known spectral lines from calibration sources, like arc lamps or celestial objects with well-characterized spectra (in this work, Argon and Xenon arc lamps are used). By comparing the observed positions of these lines with their reference wavelengths, astronomers can create a calibration function. This function accounts for any systematic shifts in the observed wavelengths, enabling the conversion of raw data into accurate wavelength values. Wavelength calibration is fundamental in enabling quantitative analysis and facilitating meaningful comparisons.

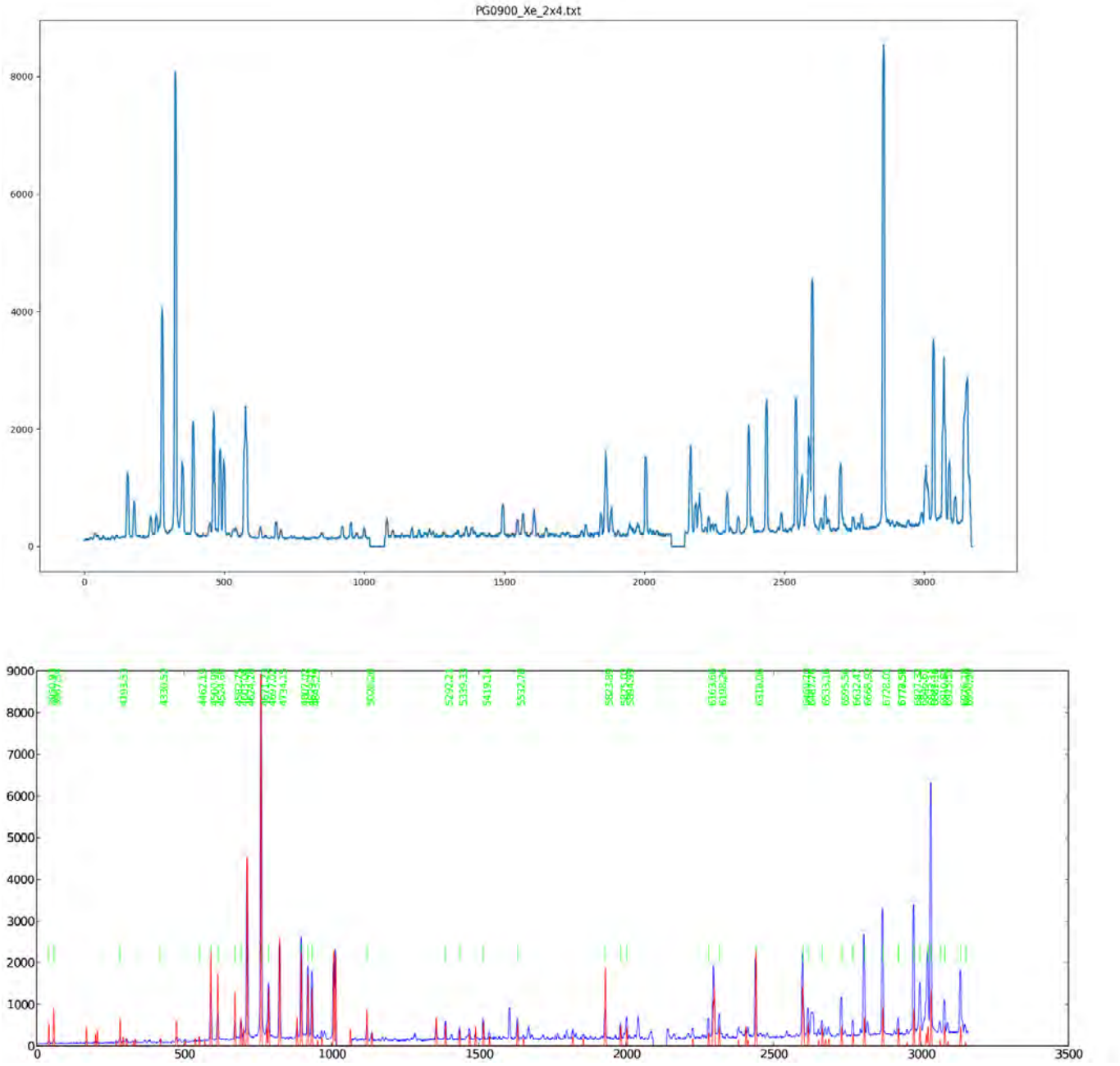


**Figure 9:** Top: Arc spectrum of object 05777 in the XMMLSS field, showcasing distinct spectral lines. Bottom: Line atlas correlated with Xenon at a grating of 14.373, providing a reference for precise wavelength calibration in astronomical spectroscopy. It must be noted that the area of interest in the top image is between 0 and a little over 500, while this region presents itself between 500 and 1000 in the bottom image.

In Figure 9, by running **rss_mos_create_arc_model mbxgpP201911030068.fits** within the 05777 products folder, the top plot is produced so as to generate the produced arc model. This is done through the use of the RSSMOSPipeline discussed in the following Subsection. The bottom

**Table 1:** Table representing the quasars used for this study along with their characteristics. The parameter CLASS STAR was not available at the time of the original SALT proposal, this is why not all values follow the condition CLASS STAR $> 0.9$.

| Target | RA | DEC | CLASS STAR | R band magnitude |
|---|---|---|---|---|
| cosmos 0057482 | 10:01:13.84 | +01:40:00.6 | 0.874844 | 21.1 |
| cosmos 0081813 | 10:01:47.40 | +01:41:44.3 | 0.980716 | 22 |
| cosmos 0140400 | 10:02:08.55 | +01:45:53.6 | 0.979805 | 21.6 |
| cosmos 0213139 | 10:02:08.80 | +01:50:58.4 | 0.980775 | 22 |
| cosmos 0334278 | 09:58:21.14 | +01:59:18.6 | 0.897453 | 21.8 |
| cosmos 0336769 | 09:59:28.45 | +01:59:34.7 | 0.439732 | 21.6 |
| cosmos 0356287 | 10:01:41.41 | +02:00:50.9 | 0.935548 | 21.7 |
| cosmos 0452303 | 10:01:18.78 | +02:07:29.8 | 0.844386 | 21.9 |
| cosmos 0604728 | 10:00:56.70 | +02:17:20.9 | 0.975479 | 21.2 |
| cosmos 0606164 | 09:57:58.40 | +02:17:29.1 | 0.980741 | 21.6 |
| cosmos 0913761 | 10:02:32.49 | +02:38:59.7 | 0.825146 | 21.1 |
| cosmos 0950734 | 10:00:25.06 | +02:41:28.4 | 0.87486 | 21.4 |

image is the arc lamp of Xenon at a grating of 14.373 within the Line Atlas (https://astronomers.salt.ac.za/data/salt-longslit-line-atlas/).

## 3.3 RSSMOSPipeline

The pipeline used in this instance is known as the RSSMOSPipeline, developed by Matt Hilton as part of work done by Hilton et al. [2018]. It is used for reducing both longslit and multi-object spectroscopy from the Robert Stobie Spectrograph (RSS) on SALT. For this work however, the RSSMOSPipeline is used for the sole purpose of longslit spectroscopy.

## 3.4 Running the pipeline

A particular arc lamp had to be selected for each observation. In the case of these targets, argon and xenon were to be used. Once this was done, the *products* folder was then run through the pipeline. This was done in the following way:

- An appropriate arc lamp was chosen.
- **rss_mos_reducer 06061/ reduced all** was run. This essentially reduces the longslit data found in the folder named 06061.

- In the case when the slit belonging to the quasar was not found, **rss_mos_reducer 06061/ -T 1 reduced all** was then ran. Subsequently, the use of (-T 1) allowed for an increase in the number of slits produced and was thus helpful in identifying fainter sources that may have been missed.

During the reduction process, the obtained data is organized into relevant folders. One of these folders, titled *reduced*, contains important data products. Within the *reduced* folder, there is a subfolder called *diagnostics*, which includes individual exposures of each slit and the corresponding sky checks. Figure 10 illustrates one of the reduced SALT spectrum that were used.

In the figure, you can observe squarish troughs around 5900 and 7000, which correspond to gaps in the detector known as chip gaps. These gaps do not receive any emission. The wavelength scale is measured in Angstroms. Additionally, the strong, narrow peaks in the figure represent background noise. It is worth noting that these peaks could also be caused by cosmic rays that were not adequately subtracted during the pipeline processing.

This procedure of organizing the data and examining individual exposures and their characteristics allows for a thorough analysis and understanding of the emission line data. It helps identify any instrumental effects, such as chip gaps, and provides insights into the presence of background noise and potential cosmic ray contamination.
Figure 11 illustrates the implementation of the blind offset technique by depicting three reference bright sources circled in red. These reference sources serve a crucial purpose in the observation as they are used in conjunction with the target of interest at the center to apply the blind offset technique. This technique is employed to determine the precise position or coordinates of the target object on the celestial sphere, even though it is too faint to see in the SALT acquisition image. Figure 12 shows a side by side comparison between the target's data representation and its finder chart. It's important to note that the data representation is not a conventional image with spatial dimensions on both the x and y axes. The x-axis in this representation corresponds to the wavelength dimension, indicating the range of wavelengths or frequencies being measured. On the other hand, given that this is a 2D spectrum, the y-axis represents the spatial axis that corresponds to the position of the target along the slit. This way of comparing the source is useful in that it helps identify each individual slitlet generated by the RSSMOSPipeline shown by the green horizontal lines in the left image. An example of the emission lines that were used to find the redshift of each source is shown in Figure 13. Unfortunately, only 1 source was found to have a spectroscopic redshift that matches the photometric redshift already at hand (described in Section 2.1). Table 2 compares the known photometric redshifts and the calculated spectroscopic redshifts

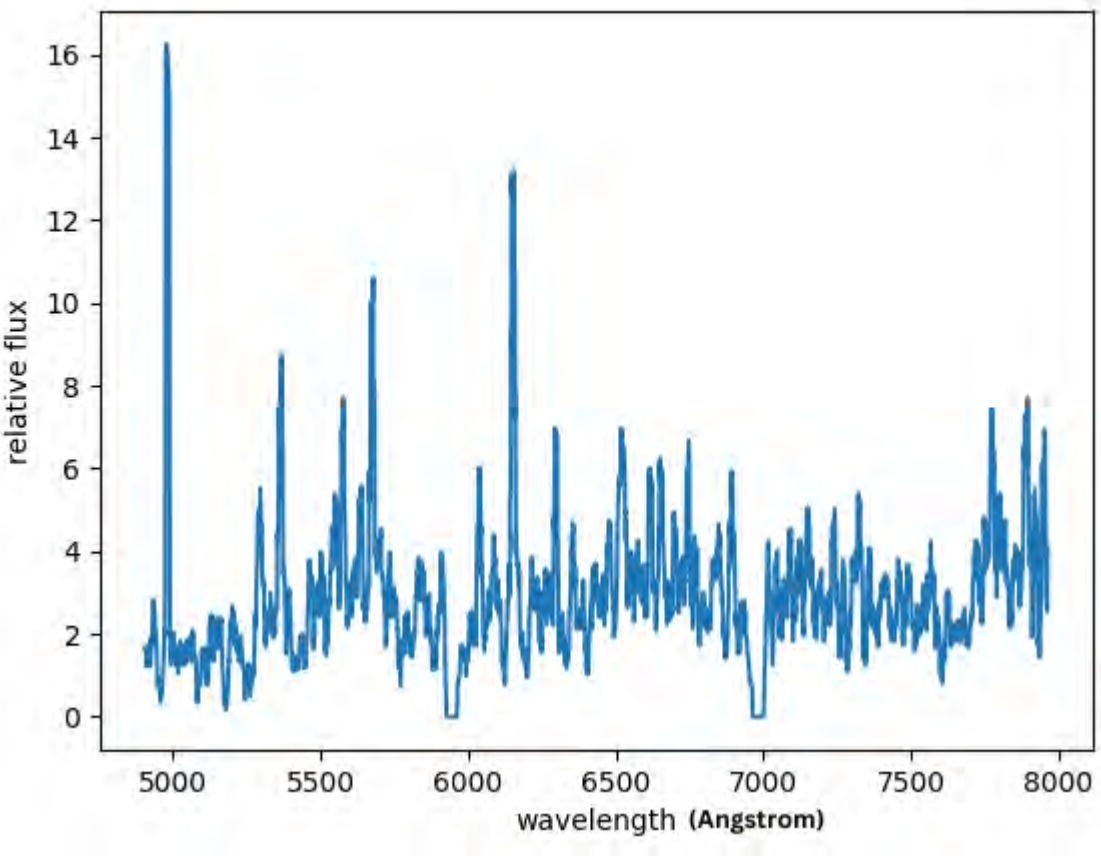


**Figure 10:** An example of one of the used SALT spectra that has been reduced.

attained for the 10 targets found within the COSMOS field.

Acquiring the spectroscopic redshift involves utilizing the redshift formula,

$$\lambda_o/\lambda_e = 1 + z \tag{7}$$

where $z$ represents the redshift, while $\lambda_o$ and $\lambda_e$ showcase the observed and emitted wavelengths, respectively. In this specific case, two observed wavelengths, 6530A and 5310A, were chosen based on their association with the 0606164 target. Please see Figure 13 for associated stacked exposures. The ratio of these observed wavelengths, 6530/5310, calculated to be 1.2298. By comparing this ratio to known emission line ratios, a potential match of 1.232 was identified, corresponding to emission lines attributed to $[CIII]_{1909}$ and $CIV_{1549}$. Using the emission line of $[CIII]_{1909}$, the redshift was calculated as $z = 6530/1909 - 1 = 2.42$. This method offers a straightforward way to estimate redshift from observed wavelengths, allowing for the identification of specific emission

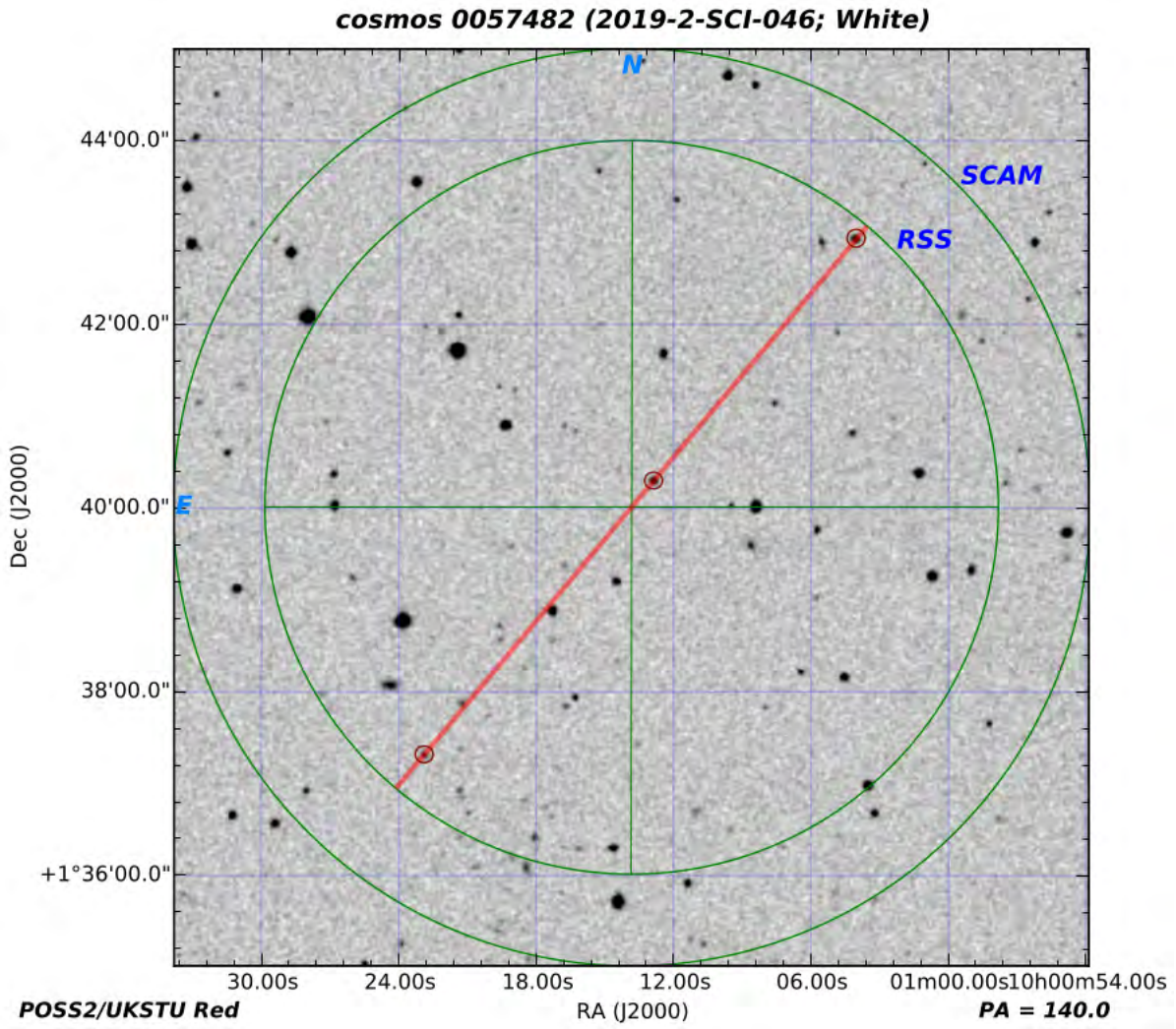


**Figure 11:** An example of a finder chart used to locate a quasar at the center of the plot relative to other optical sources. The red line indicates the position angle of the longslit and the circled points are bright sources that lie on the same line.

lines and, consequently, the determination of redshift values. However, it is important to note that this process assumes a specific line identification, and the accuracy of the redshift estimation depends on the correctness of this assumption. Additionally, different emission lines or a more complex spectral composition could introduce challenges in accurately matching observed ratios to known emission line ratios. Figure 14 is an example of the skyCheck image that is a measure of the relative flux against the wavelength. The black vertical lines are the expected sky emission lines. These dashed lines lining up with some of the green line's emission points prove that the wavelength calibration worked well.

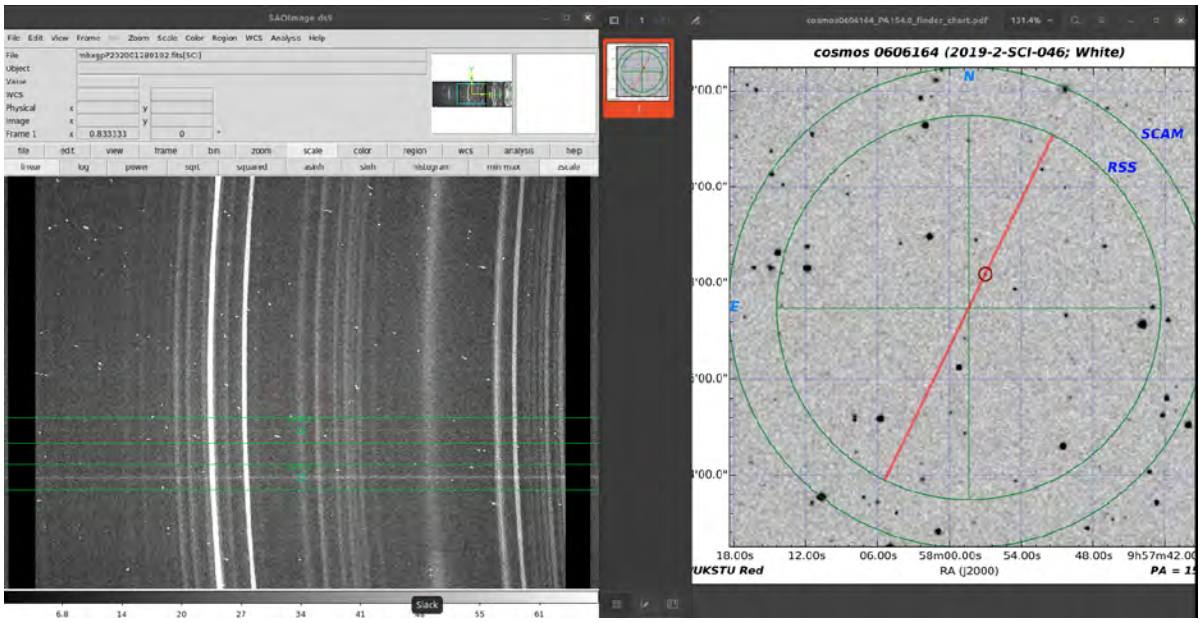


**Figure 12:** A comparison between an image of a quasar with ID 0606164 at an RA of 149.493 degrees and Dec of 2.291 degrees vs its finder chart equivalent.

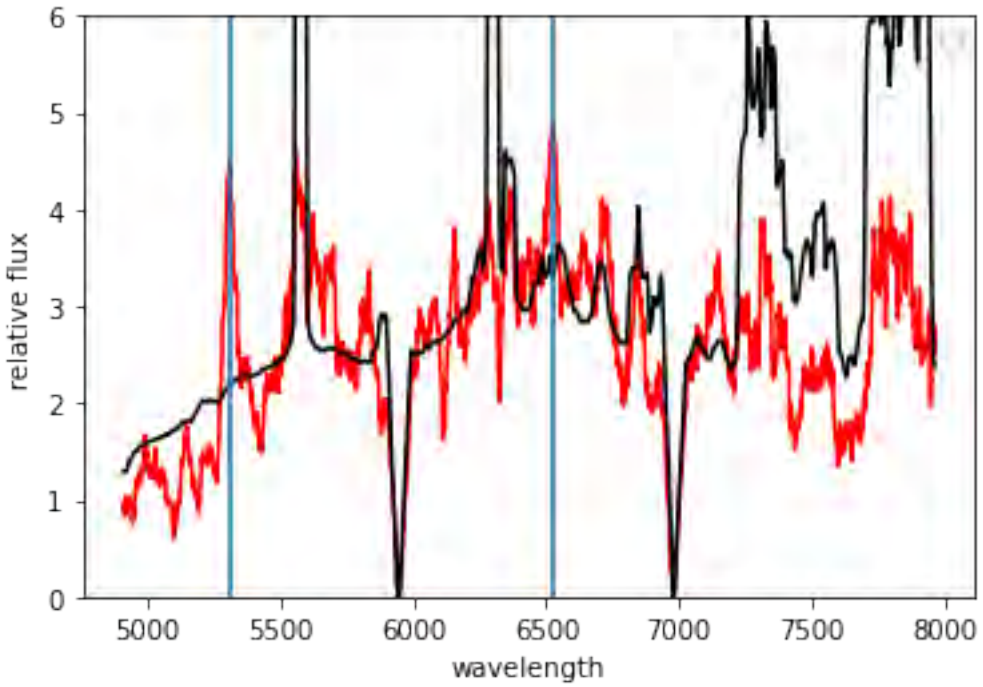


**Figure 13:** Stacked exposures given by the red line, sky background represented by the black line and emission line points given by blue vertical lines. Blue, vertical lines are at the wavelengths 5310 A and 6530 A. The RSSMOSPipeline extracts the sky-spectrum so that this can be subtracted from the spectrum at the position of the target. In total, there were three exposures per target that were taken.

| Target | Photometric z | Spectroscopic z |
|---|---|---|
| 0057482 | 1.64 | 0.9 |
| 0140400 | 2 | 0.54 |
| 0213139 | 1.72 | NA |
| 0334278 | 1.72 | 0.93 |
| 0356287 | 2.08 | 0.4 |
| 0604728 | 1.92 | 1.05 |
| 0606164 | 2.48 | 2.43 |
| 0913761 | 1.92 | NA |
| 0950734 | 1.88 | NA |

**Table 2:** Quasar targets with their corresponding photometric and spectroscopic redshifts. What is witnessed in the this table is a clear discrepancy between the photometric redshifts and the calculated spectroscopic redshifts. Values that are labeled as NA are because of either a shift in calibration or an undetectable source The only calculated spectroscopic redshift that corresponds to photometric redshift is target 0606164.

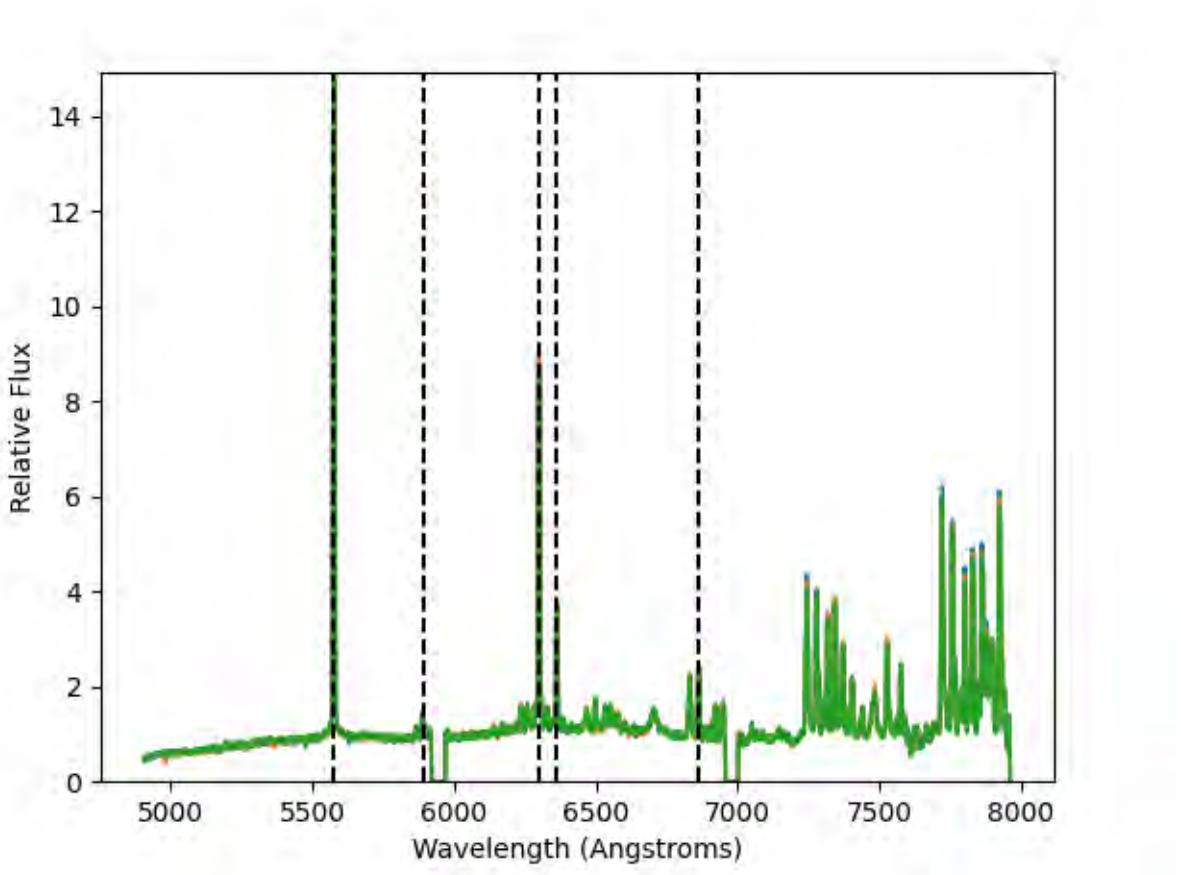


**Figure 14:** Where sky emission lines (green lines with overlapping dashed black lines) are expected to lie. The heavily obscured orange and blue lines are the two other exposures per target used for this work.

# 4 Analysis of the MIGHTEE radio images

> "I do not think that the radio waves I have discovered will have any practical application"
>
> Heinrich Hertz

## 4.1 Radio interferometry

Radio interferometry plays a crucial role in radio astronomy as it enables deep and detailed observations. Unlike single dish telescopes, radio interferometers like MeerKAT leverage the combined collecting area of multiple smaller dishes, resulting in exceptional sensitivity. The 64 dishes of MeerKAT, while individually not possessing a large surface area, collectively contribute to its remarkable resolution. Figure 15 provides an example of a radio interferometer setup. The resolution of these telescopes, on the other hand, is determined by the baseline, which represents the distance between the dishes. In radio astronomy, interferometers consist of a network of telescopes that operate as a cohesive unit. This technique offers a practical solution by obviating the need for constructing prohibitively large single telescopes.

### 4.1.1 Fourier transform

The Fourier transform is a mathematical technique that allows us to analyze a function in terms of its frequency components. It decomposes a function, which is typically a signal in the time domain, into a series of complex exponential functions in the frequency domain.

For any complex function $f(x)$ of a real variable $x$, under certain conditions, the Fourier transform provides a representation of the function in terms of its frequency content. The function $f(x)$ should have only finite discontinuities and be integrable, meaning it has a well defined integral over its domain.

The Fourier transform of $f(x)$, denoted as $F(s)$, is defined by the integral:

$$F(s) = \int_{-\infty}^{\infty} f(x) e^{-2\pi i s x} dx \tag{8}$$

This equation expresses the transformation of the function $f(x)$ from the time domain to the frequency domain. The parameter $s$ represents the frequency variable.

The integral takes the complex exponential function, characterized by the term $e^{-2\pi i s x}$, which

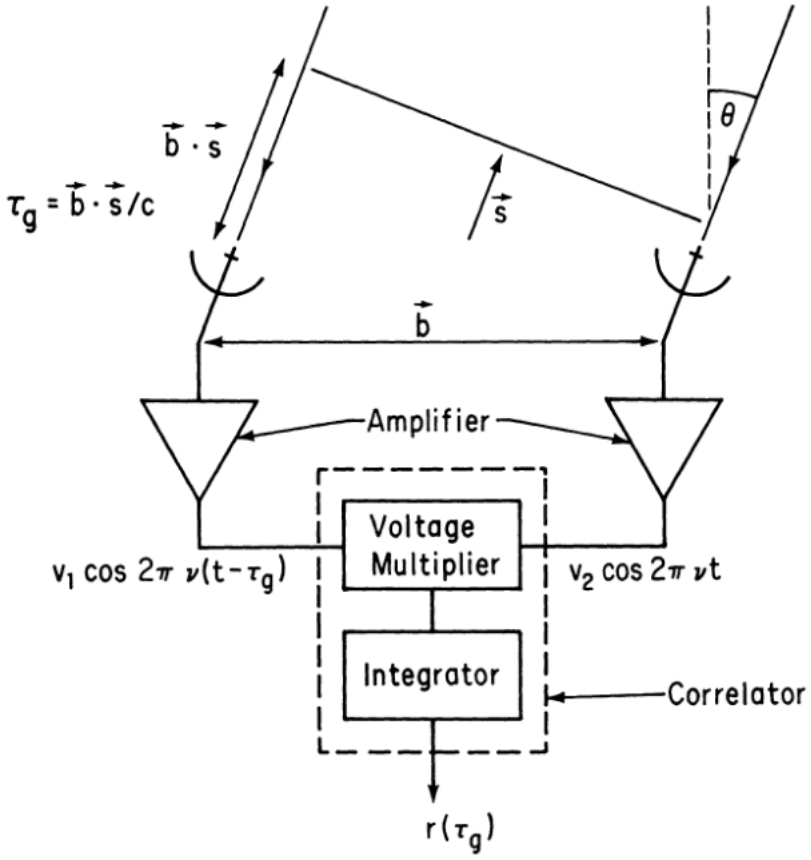


**Figure 15:** Schematic diagram of a two-point interferometer, subtended by a baseline given by $\vec{b}$ [Thompson, 1999]. The wavefront is in the $\vec{s}$ direction, at an angle of $\theta$. $\tau_g$ is known as the geometrical delay and $r(\tau_g)$ is the output of the correlator.

represents a sinusoidal oscillation at frequency $s$, and multiplies it by the function $f(x)$. The result is integrated over the entire range of $x$, from negative infinity to positive infinity

The inverse transform, denoted as $f(x)$, allows us to recover the original function $f(x)$ from its frequency representation $F(s)$. It is defined as:

$$f(x) = \int_{-\infty}^{\infty} F(s) e^{-2\pi i s x} ds \tag{9}$$

This equation represents the transformation from the frequency domain back to the time domain. It involves integrating the product of the frequency spectrum $F(s)$ and the complex exponential function with respect to the frequency variable $s$.

### 4.1.2 Visibilities

Interferometric visibility refers to the Fourier transform of the sky brightness, capturing the spatial frequency information of the observed source. To convert visibilities into an image, additional steps and calibrator observations are required. These include antenna gains, bandpass response, atmospheric effects, and phases using observations of point and spectral calibrators, phase calibrators, and flagging/editing for RFI, ensuring accuracy in the reconstructed image. The measured visibilities, denoted as $V_\nu(u, v)$, can be transformed into an image represented by $I_\nu(l, m)$ using the equation given below:

$$I_\nu(l, m) = \int \int V_\nu(u, v) e^{i2\pi(ul+vm)} du dv \tag{10}$$

This mathematical expression demonstrates the Fourier transform operation performed over the spatial frequency domain, integrating the visibilities with respect to the variables $u$ and $v$. Through this transformation, the image $I_\nu(l, m)$ is constructed, enabling the visualization and analysis of the observed data. The Van Cittert-Zernicke (vCZ) theorem in physical optics states that the observed interferometric visibilities, denoted by $V$, are related to the sky brightness distribution, represented by $I$, both of which depend on frequency, $\nu$. This theorem establishes a fundamental connection between the measured visibilities and the underlying brightness distribution of the observed object in the field of physical optics.

### 4.1.3 Image reconstruction

The two-element interferometer, as depicted in Figure 15, serves as a fundamental unit in radio interferometry. Arrays like MeerKAT comprise multiple such interferometers, with each antenna pair functioning as a two-element interferometer. These systems enable the measurement of points in uv-space, known as visibilities, which are susceptible to instrumental effects such as antenna gains, RFI, and thermal noise. The vCZ theorem establishes that these visibilities represent a 2D Fourier transform (Equation 10) of the sky image, laying the groundwork for image reconstruction.

However, due to the incomplete sampling of the uv-plane, the inverse 2D transform does not directly yield the original sky image but rather produces a "dirty image" denoted as $I_{dirty}$. This image is a convolution of the true sky brightness by the Point Spread Function (PSF), as dictated by the Fourier convolution theorem. Consequently, converting measured visibility data to meaningful information involves several steps. This process includes calibrating antenna gains, addressing bandpass and atmospheric effects through calibrator observations, applying corrections to the measured data, and generating dirty images via Fourier transforms. Furthermore, deconvolution

algorithms like CLEAN are employed to mitigate the effects of the PSF, enhancing the accuracy of the reconstructed images. MeerKAT operations may also necessitate direction-dependent calibration, although addressing this complexity extends beyond the scope of this thesis.

## 4.2 MeerKAT

One of the most anticipated advancements in the field of radio astronomy is the construction of the Square Kilometre Array (SKA), which represents a significant leap forward in telescope technology. Building upon the successes of precursor telescopes like the Karoo Array Telescope (KAT) with 7 dishes and the recently completed MeerKAT, the SKA is poised to become the most powerful operational radio telescope. Radio telescopes are designed to capture and study the radio portion of the electromagnetic spectrum, and it is within this frequency range that interferometric techniques excel. MeerKAT, comprising a strategically positioned array of 64 dishes with a diameter of 13.5 meters, leverages interferometry to enhance our ability to observe and study radio emissions from celestial sources, both nearby and distant.

## 4.3 The MIGHTEE survey

One of the Large Survey Projects (LSPs) conducted through the use of this radio telescope is the MeerKAT International Gigahertz Extragalactic Exploration (MIGHTEE) survey, as highlighted by Jarvis et al. [2017] and visually depicted in Figure 15. The MIGHTEE survey (shown in Figure 16) encompasses a vast area of 20 square degrees across gigahertz frequencies and achieves micro-Jansky sensitivities. This comprehensive survey aims to collect valuable data on radio continuum, spectral line, and polarization information, enabling a deeper understanding of the evolution of AGN and SF, as well as the behavior of neutral hydrogen and cosmic magnetic fields. In the context of this study, the focus is specifically on a portion of the MIGHTEE survey known as the COSMOS field, which spans an area of 1.5 square degrees. Exploring the COSMOS field provides the advantage of accessing a rich collection of multi-wavelength data associated with the MIGHTEE survey. This combination of radio observations and multi-wavelength data sets the stage for investigating the radio emission of RQ candidates, building upon previous work conducted by White [2015].

## 4.4 Radio data extraction

Upon identifying the optical/NIR AGN candidates, radio data of the same field was used to find an estimate of the radio flux density emanating from the selected targets. The radio measurements are based on a single pixel per source presented in Jy/beam, reflecting the flux density within each

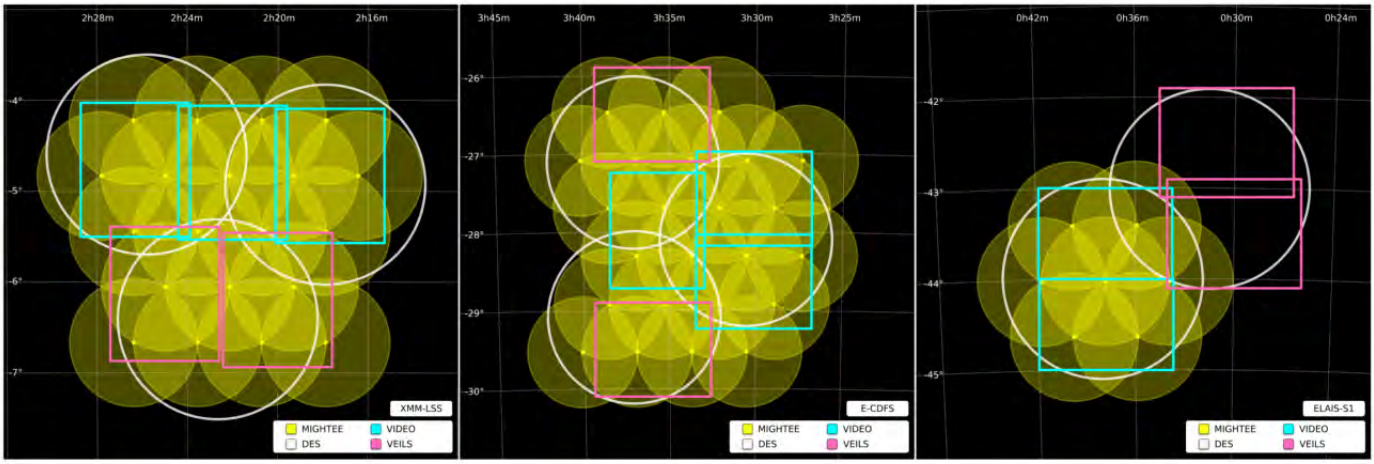


**Figure 16:** The MeerKAT International Gigahertz Extragalactic Exploration (MIGHTEE) survey includes three fields (XMMLSS, E-CDFS, and ELAIS-S1) as part of its scope, as described by Jarvis et al. [2017]. In this figure, the MIGHTEE survey regions are highlighted by yellow circles, while the Dark Energy Survey regions are depicted by white circles.

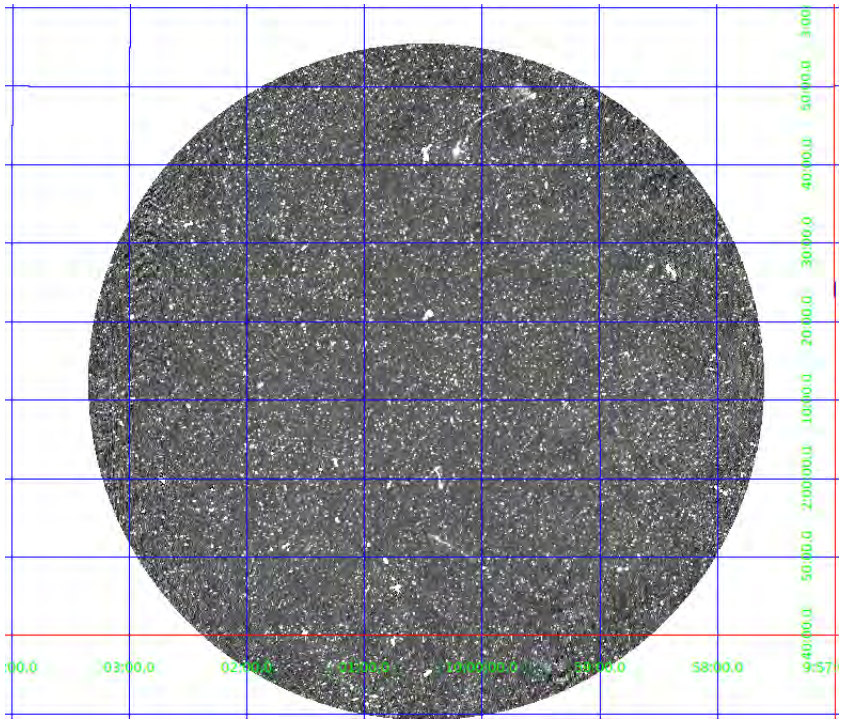

**Figure 17:** Image of the COSMOS field.

beam. This metric is appropriate for our point sources, as they exhibit negligible spatial extent on the scale of the beam. Using single-pixel flux densities is acceptable for point-like radio sources due to their compact nature. The emission from these sources can be adequately captured within a

single pixel, and their characteristics align with the assumptions of point-source modeling. Through this, a radio estimation of SFR can be done against optical/NIR SFR. The following procedure was used to attain source flux densities from the COSMOS field shown in Figure 17:

- Positions (the RA and Dec) of the optical/NIR selected sample of AGN were read in.
- The world coordinate system (WCS) coordinates were then converted to pixel coordinates.
- The resulting pixel values, which indicate the radio brightness, were read in as counts.

The offset flux densities were generated using a technique known as the blind offset method. This method involves measuring the flux density values at nearby regions in the image, away from the AGN candidates. This involves measuring the background or noise level in an image by selecting positions that are relatively noise-dominated and sufficiently far from significant sources of signal. These positions are usually chosen based on their proximity to the regions of interest within the image. In this method, multiple offset positions are commonly used for each position of interest. For this work, an angular separation of 30 arcseconds was used. The goal is to obtain a robust estimate of the noise level in the image, and using several offset positions helps to account for any local variations or artifacts that may affect the noise measurement. By averaging the measurements from multiple offset positions, a more accurate and reliable estimate of the background or noise level is obtained, which can then be used for statistical analysis and for quantifying the noise so that an estimate of how well-detected the sources are in the radio. The purpose of generating the offset flux densities is to provide a reference or baseline measurement of the background radio emission. By comparing the flux densities of the AGN candidates to the offset values, we can assess the significance of the AGN emission relative to the background. This analysis helps us determine the strength and detectability of the AGN candidates in relation to the surrounding radio emission.

## 4.5 Determination of the radio luminosity

The radio luminosity was attained using the following relation,

$$L = 4\pi \frac{FD^2}{(1+z)^{1+\alpha}} \tag{11}$$

In the equation, the symbols represent the following:

- $L$: Radio luminosity, which represents the total power emitted by the radio source.
- $F$: Flux density, which refers to the amount of radio emission received per unit area.
- $D$: Luminosity distance, which is the distance between the observer and the source taking into account the expansion of the Universe.
- $z$: Redshift, which measures the shift in the wavelength of light due to the expansion of the Universe. It indicates how much the source's light has been stretched or shifted towards longer wavelengths.
- $\alpha$: Spectral index, which characterizes the dependence of the source's flux density on frequency. It describes how the flux density changes as a function of wavelength or frequency.

The units of the variables in the equation are as follows:

- $L$: Usually expressed in units of watts (W) or ergs per second (erg/s).
- $F$: Typically given in units of flux density, such as Janskys (Jy), where 1Jy = $10^{-}26\text{W/m}^2\text{/Hz}$.
- $D$: Measured in units of length, such as meters (m) or parsecs (pc).
- $z$: A dimensionless quantity since it represents a ratio of wavelengths.
- $\alpha$: A dimensionless quantity as it is a spectral index.

Here, the luminosity distance refers to the distance which the observed flux is from an object, while the spectral index is the variation of intensity with the frequency of the continuum emission from radio sources and is -0.7, which is a typical value for synchrotron radiation. The equation relating luminosity distance to observed flux is given by the cosmological luminosity distance formula:

$$D_L = \sqrt{\frac{L}{4\pi F}} \tag{12}$$

$D$ is dependent on the absolute magnitude ($M$) and the apparent magnitude ($m$) of an astronomical object in the following manner:

$$M = m - 5\log_{10}\frac{D}{10pc} \tag{13}$$

The distribution of radio flux density is thus given by Figure 17. The Gaussian in the plot repre-

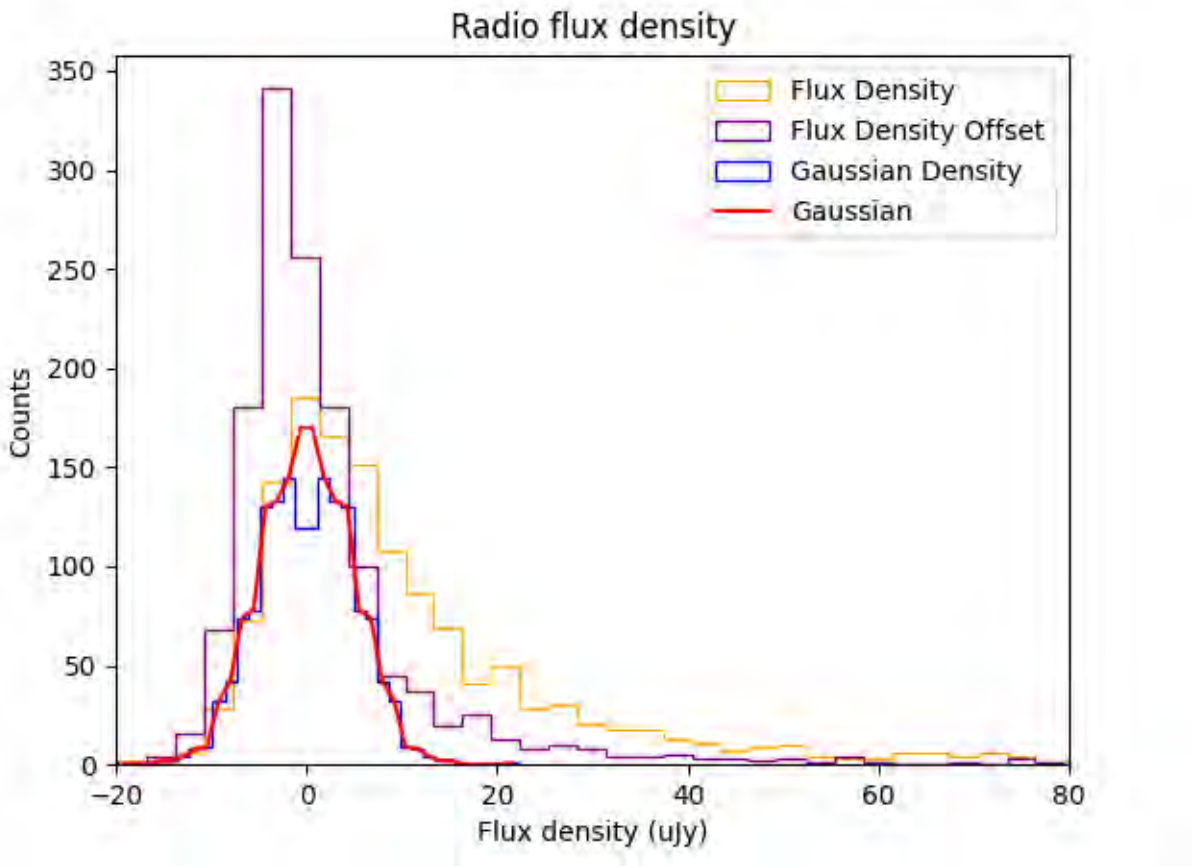


**Figure 18:** The figure illustrates the radio flux density distribution, with the orange curve representing the flux density histogram and the purple curve depicting the corresponding offset. The blue curve denotes the Gaussian density associated with the data, derived from both positive and negative offsets. An attempt at fitting the Gaussian tied to the Gaussian density is depicted through the red line, which was attained with the use of a curve-fitting algorithm.

sents a fitted Gaussian distribution, which is a mathematical function used to model the observed distribution of radio flux density. We perform this fitting to characterize the shape and properties of the flux density distribution, such as its central tendency and dispersion.

The purpose of fitting a Gaussian to the distribution is to extract meaningful information and parameters from the data. The Gaussian fitting allows us to estimate important quantities such

as the peak value (representing the most common flux density), the width (indicating the spread or variability of the flux density values), and the overall shape of the distribution. By fitting a Gaussian, we can quantitatively describe the statistical properties of the observed radio flux density distribution.

Thermal noise refers to the inherent noise present in the radio observations due to the random fluctuations in the electronic components of the observing system. It is a type of noise that is intrinsic to the measurement process and arises from thermal effects. On the other hand, confusion noise arises from the presence of multiple radio sources within the observed region. It occurs when the angular resolution of the observation is not sufficient to distinguish between individual sources, resulting in the overlapping or blending of their emission.

In the context of the plot of the distribution of radio flux density, the fitting of a Gaussian helps us to quantify the characteristics of the observed flux density distribution, providing insights into the statistical properties of the radio sources. By understanding the nature of the flux density distribution and differentiating between thermal and confusion noise, we can better analyze and interpret the data, and make accurate conclusions about the properties and behavior of the radio sources in question.

To estimate the noise level of the radio images, offset positions were used as a reference to measure the background or baseline level of the observed region. The offset positions are typically chosen to be sufficiently far away from any significant radio sources or emission, ensuring that they represent a relatively noise-dominated region. By measuring the flux density at the offset positions, we obtain an estimate of the background or noise level in the radio images. This is important because it allows us to separate the true signal from the noise and quantify the significance of the detected sources.

In Figure 18, the orange histogram represents the flux density values observed at the positions of interest. On the other hand, the blue histogram represents the Gaussian density. Using offset positions helps in understanding and characterizing the noise properties in the radio images. It allows us to estimate the noise standard deviation or the typical variation in the background level, which is crucial for statistical analysis and identifying genuine sources of interest. By differentiating between the noise level estimated from the offset positions and the actual flux density measurements at the positions of interest, we can identify sources that exceed the expected noise level and are therefore more likely to be true radio sources rather than random fluctuations or

noise artifacts. Finally, the analysis of the radio flux density distribution, with a fitted standard deviation and image noise estimate of $5 \times 10^{-6}$ Jy/beam, allows us to accurately quantify the noise properties and identify justifiable radio sources. In this study, 91.53 percent of the sample have a radio flux density that is above $3\sigma$. Work done by White et al. [2017] highlight that the accretion process accounts for 80 percent of the radio luminosity with a $2\sigma$ threshold, it suggests a high confidence level that this process is indeed a major contributor to the observed radio emissions across the studied objects. These numerical values are essential for statistical analysis and provide a foundation for confidently distinguishing real radio sources from noise artifacts in the observed data.

## 4.6 A comparison of SFRs

As highlighted earlier, the optical/NIR distribution of the selected sources was conducted through the utilization of a *gJKs* colour-colour plot. This approach facilitated the selection of the sample, while the SFRs derived from the optical/NIR photometry were a result of the fitting of SED templates, which also provided the redshift values tied to these quasars (see Section 2.1).

The estimation of SFR from radio observations relies on an empirical relation established by Yun et al. [2001] in their study titled "Radio properties of infrared-selected galaxies in the IRAS 2 Jy sample". Here, this relation is used by assuming that all the emission is due to SF and is given by,

$$SFR(M_{\odot}yr^{-1}) = 5.9 \pm 1.8 \times 10^{-22} L_{1.4GHz}(WHz^{-1}) \tag{14}$$

The relation quantitatively connects the radio luminosity at a specific frequency to the SFR. It was derived by analyzing the properties of galaxies selected from the IRAS 2 Jy sample, which consists of IR-selected galaxies. The sample was carefully examined to understand the relationship between their observed radio luminosity and the associated SFRs. The resulting empirical relation provides a useful tool for estimating the SFR based on radio observations.

The determination of the dominant radio emitter, whether it is AGN or stellar contributions, is based on the understanding that detectable SF related radio-emissions are commonly associated with specific types of stars, particularly those with strong magnetic fields or active coronae, as well as certain nearby stars. However, radio emissions can also originate from other sources too. It is important to note that the radio emission we are interested in, which is associated with SF, is primarily attributed to supernova remnants rather than the stars themselves. In so doing, one can trace the SFR using two independent means, as first shown by Helou et al. [1985]. As such, this

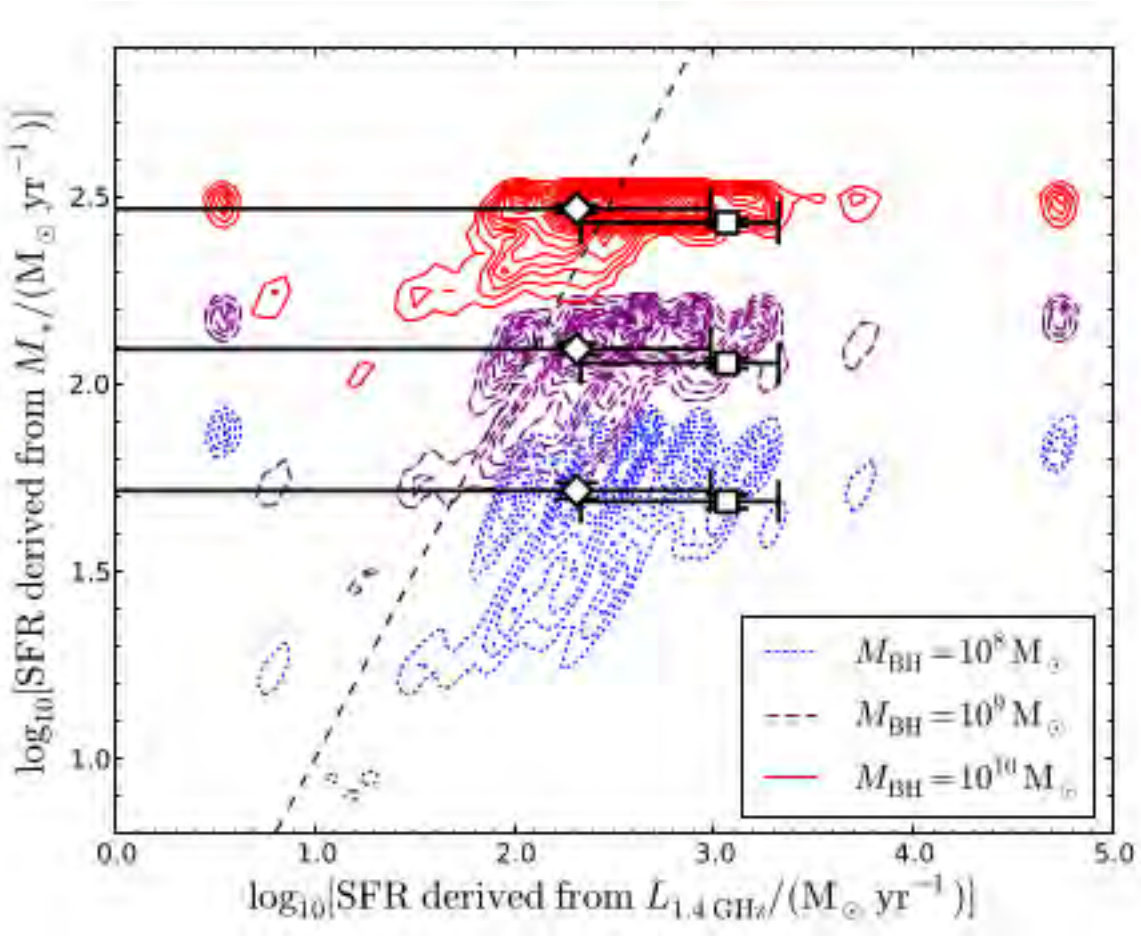


**Figure 19:** The image illustrates the relationship between the SFR calculated using estimated stellar masses for various BH masses (assuming that the quasars have host galaxies that lie on the SF-mass main sequence) and the SFR calculated from extracted radio flux density at 1.4 GHz. It presents simulated quasars as coloured contours (blue, purple, and red) based on assumed BH masses, with a dashed line indicating a one-to-one relation between SF and radio emission.
[White et al., 2015].

SFR comparison is better suited to detecting anything that deviates from its 1:1 linear nature. An example of work that has shown a deviation from this relation comes in the study of RQQs done by White et al. [2015]. Through this, one can clearly see the radio contribution that AGN activity has in Figure 19. In this study, the deviation from the expected 1:1 relation is demonstrated in Figure 20. Objects that lie on the relation have properties that are consistent with SFGs. However, it is important to note that we are not comparing the radio emission with the optical/NIR emission directly. Instead, we are comparing two estimates of the SFR that are derived from different parts of the electromagnetic spectrum.

| | **Radio Luminosities** ($\mathrm{WHz}^{-1}$) | **Redshifts** | **SFR**$_R(\mathrm{M}_\odot/yr)$ | **SFR**$_O(\mathrm{M}_\odot/yr)$ |
|---|---|---|---|---|
| **Range** | $3.91 \times 10^{24}$ | 4.32 | 2305.69 | 3.80 |
| **Median** | $4.28 \times 10^{22}$ | 0.92 | 25.27 | 1.29 |
| **Lower Limit** | $3.89 \times 10^{19}$ | 0.12 | 0.023 | 0.002 |
| **Upper Limit** | $3.91 \times 10^{24}$ | 4.4 | 2305.71 | 3.80 |

**Table 3:** Properties of the sample used for this work, where $SFR_R$ and $SFR_O$ are the radio and optical/NIR derived SFRs respectively.

## 4.7 Interpretation of results

The absence of correlation between radio emission and optical/NIR emission, as observed through deviations from a 1:1 relation, suggests a probable association with AGN processes. This inference aligns with the findings discussed by Panessa et al. [2019], who extensively explore four primary physical mechanisms (SF, coronal emission, winds and jets) as potential contributors to radio emission in RQ AGN. SF involves high-energy phenomena associated with massive stars, such as supernovae and stellar winds, generating radio-frequency radiation. The AGN corona, an X-ray-emitting region around the SMBH, can emit radio waves through synchrotron radiation. Additionally, AGN-driven winds and outflows interact with the surrounding medium, contributing to radio signals. Collimated jets in AGN also emit radio waves through synchrotron radiation, forming another mechanism investigated by Panessa et al. [2019]. Together, these mechanisms offer a comprehensive framework for interpreting observed radio emissions in the context of AGN activity, enriching our understanding of underlying physical processes.

The exclusion of numerous sources due to non-fitted or non-physical values in radio luminosity, optical/NIR, and radio derived SFRs had to be employed in order to avoid the introduction of inaccuracies in the analysis phase and underscores the need for rigorous data selection, leaving only 516 sources for analysis. This occurred once the radio derived SFRs had been calculated.

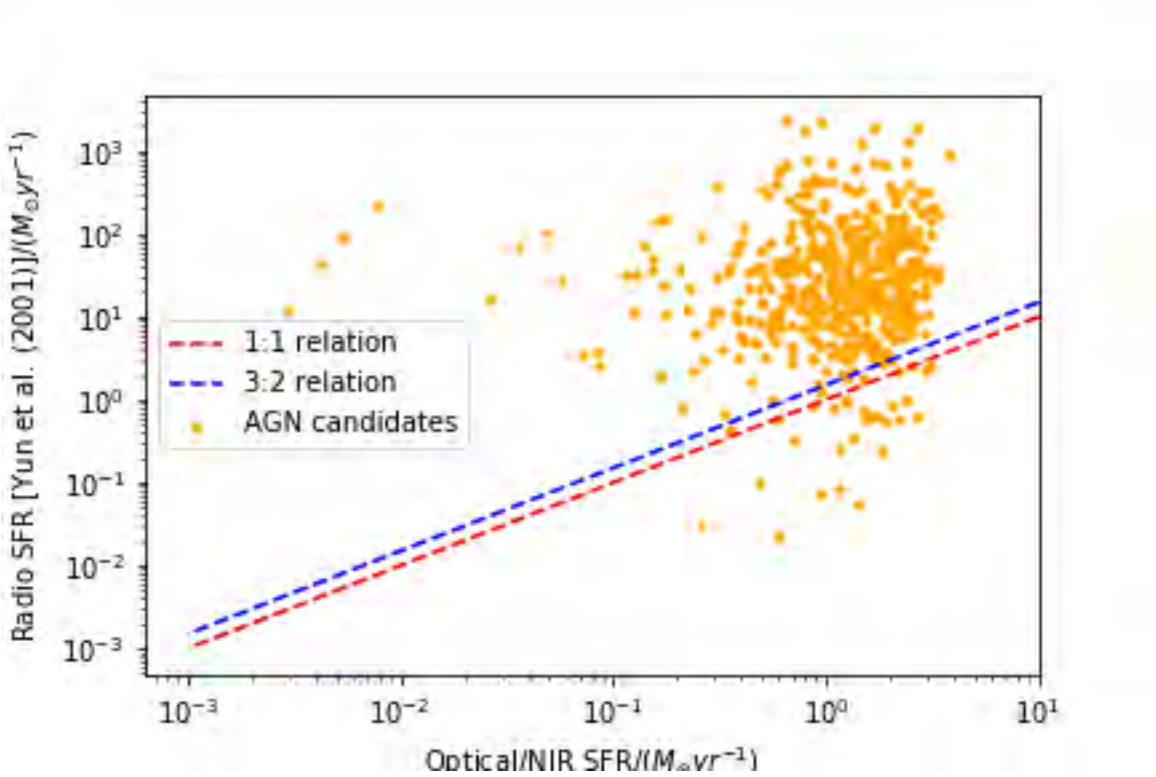


**Figure 20:** AGN sample containing 516 candidates: Two estimates of the SFR derived from different segments of the electromagnetic spectrum. The radio SFR is derived using the MIGHTEE data, while the optical/NIR SFR is based on the SALT dataset. The red dashed line represents star-forming galaxies, while the blue dashed line depicts a 3 to 2 ratio of AGN radio emission against emission that is as a result of SF (60 percent AGN and 40 percent SF).

# 5 Conclusion and future work

"I write what I like"

Bantu Stephen Biko

Work done by Kimball et al. [2011] presented results towards the characterization of the radio population of QSOs at both the faint and bright end of the radio luminosity function. They found that there are two contributors to the radio emission produced. A majority of which was said to be as a result of strong SF in the QSO host galaxies as shown in Figure 21. The data sets used are that of the 6 GHz Expanded Very Large Array observations along with a colour selected sample from the Sloan Digital Sky Survey Data Release Seven and the NRAO-VLA Sky Survey observations. Figure 21 mainly represents radio sources powered by SF (solid red curve) vs those that are powered by AGN (solid green curve). These two curves clearly show the dominance of SF at the faint end of the radio luminosity function.

My work aims to determine the contribution of radio emission from RQ AGN in comparison to the radio emission originating from SF processes. The COSMOS field was specifically chosen for its extensive collection of multi-wavelength data, providing a rich resource for analysis. The selection process for the RQ AGN in this study was based on a *gJKs* colour-colour plot. To investigate the sources, the study built upon previous work conducted by White et al. [2015], which established that AGN are the primary contributors to the radio flux density among RQQs. By comparing independent SFRs, it was confirmed that AGN predominantly account for the radio emissions, as depicted in Figure 20.

In this study, the SFRs determined by Yun et al. [2001] were compared to the SFRs derived from the established optical/NIR sample. The inclusion of optical/NIR emissions in the SFR calculation offers the advantage of accounting for older stellar populations. While the optical part of the spectrum is biased toward recent or ongoing SF, incorporating NIR data allows for the study of systems with lower mass and older stellar populations, and facilitates a broader comparison of SFRs.

The comparison of SFRs between different sources led to the conclusion that RQ AGN, as identified through the selection process, contribute significantly to the observed radio flux density. After calculating the number of sources that have a radio SFR that is 1.5× greater than the optical/NIR SFR, it was found that there are 483 sources, which is about 94 percent of the total AGN sample used. The selection procedure involved separating out AGN from star forming regions and impos-

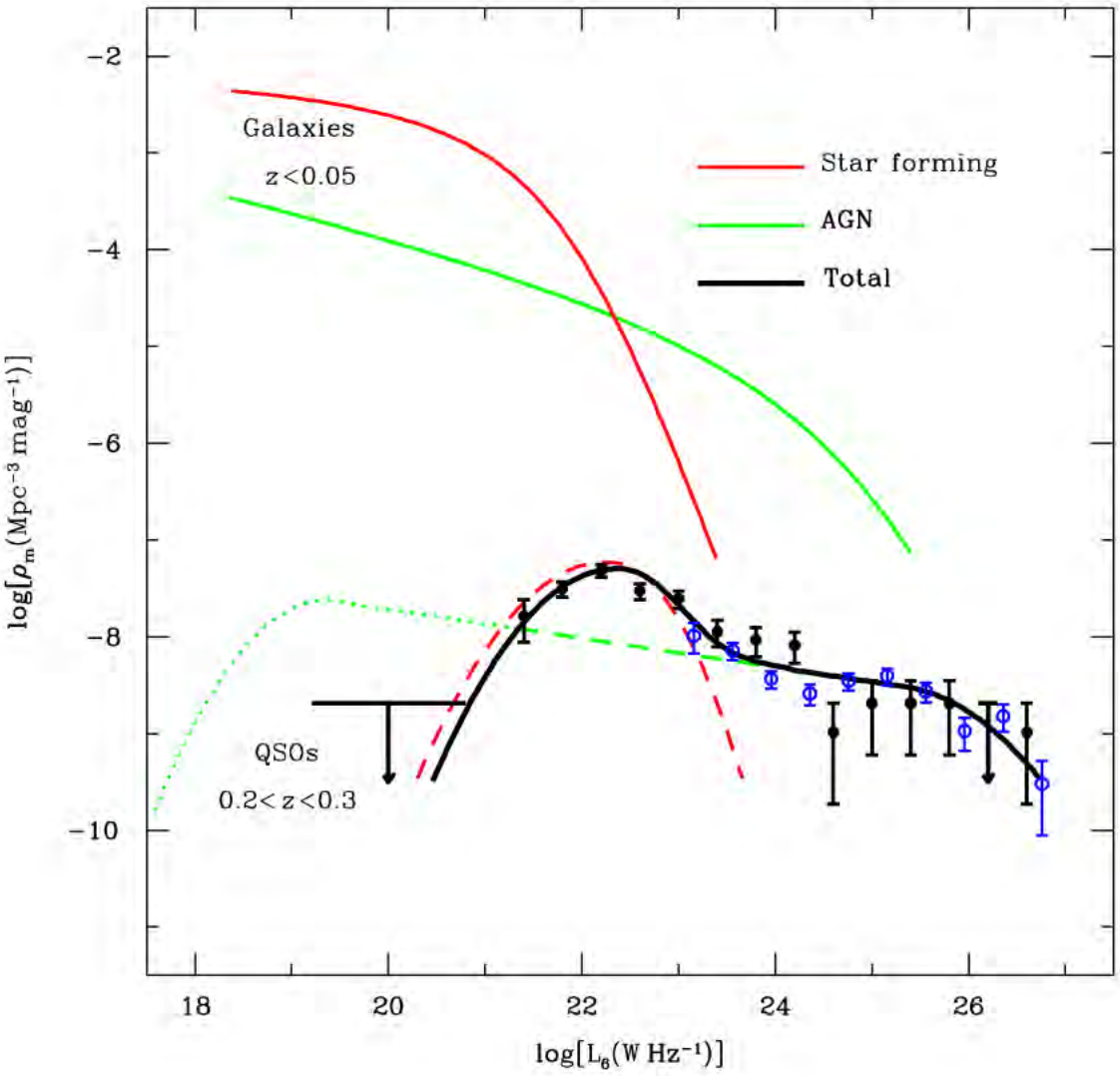


**Figure 21:** Radio sources powered by SF vs AGN. Plot extracted from Kimball et al. [2011].

ing a strict K band cut in order to investigate the objects of interest. This finding supports the notion that AGN activity plays a substantial role in radio emissions among RQQs, as opposed to SF processes alone.

Future work will be directed towards attaining large samples of photometric redshifts and the associated probabilities of each individual quasar in order to correctly propagate any errors. This will be done via their probability distribution functions. Furthermore, the relationship that AGN, galaxy formation and evolution have, may be understood better. The InfraRed Radio Correlation (IRRC), as depicted in Figure 22 and documented in White et al. [2017], serves as a valuable tool in future investigations to discern the contribution of AGN versus SF. The IRRC assists in

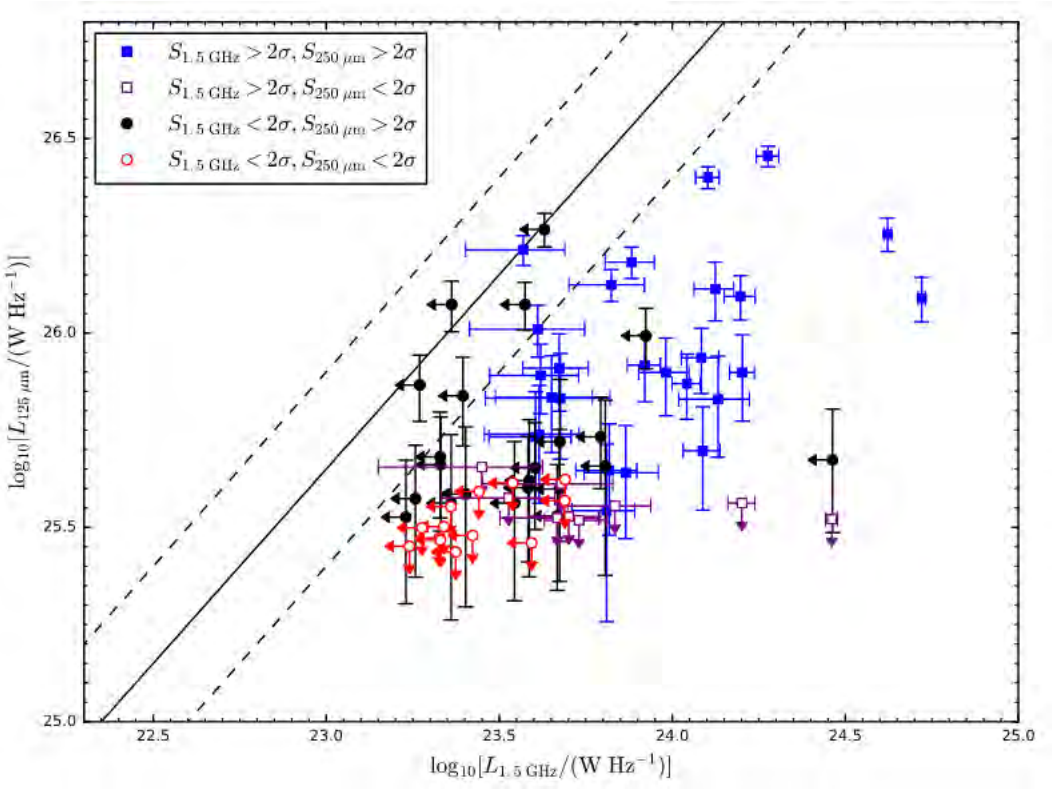


**Figure 22:** Monochromatic luminosity at rest frame 125 $\mu$m vs radio luminosity. The dashed diagonal lines represent the lower and upper bounds on $q_{125}$, 2.4 and 2.9, while the mid-point ($q_{125}$ = 2.65) corresponds to the solid line. In addition, arrows correspond to $2\sigma$ upper limits in either luminosity at rest frame 125 $\mu$m or radio luminosity for quasars undetected at $2\sigma$.

establishing the relationship between IR and radio emissions, enabling us to examine the correlation between these two properties. In the plot, we need to look for the alignment of data points, indicating a positive correlation between the IR and radio flux densities.

Based on the IRRC plot, additional calculations can be performed, such as estimating the radio flux density corresponding to a given IR flux density and vice versa. However, it is important to note that the IRRC method has its limitations, as it assumes a linear correlation and may not capture complex variations or intrinsic scatter. Alternatively, Very Long Baseline Interferometry (VLBI) can be employed as another approach for separating AGN and SF contributions. VLBI allows for high-resolution imaging and can reveal the compact radio emission associated with AGNs, aiding in their identification and differentiation from SF-dominated sources.

Another thing to be established in the future are the spectroscopic redshifts of the 8 other remaining targets.

# References


NJ Adams, RAA Bowler, MJ Jarvis, B Häußler, RJ McLure, A Bunker, JS Dunlop, and A Verma. The rest-frame UV luminosity function at $z \sim 4$: a significant contribution of AGNs to the bright end of the galaxy population. *Monthly Notices of the Royal Astronomical Society*, 494(2): 1771–1783, 2020.

S Arnouts and O Ilbert. Lephare: Photometric analysis for redshift estimate. *Astrophysics Source Code Library*, pages ascl–1108, 2011.

Rachel Bezanson, Pieter Van Dokkum, and Marijn Franx. Evolution of Quiescent and Star-forming Galaxies since $z \sim 1.5$ as a Function of their Velocity Dispersions. *The Astrophysical Journal*, 760(1):62, 2012.

Volker Bromm and Abraham Loeb. Formation of the first supermassive black holes. *The Astrophysical Journal*, 596(1):34, 2003.

Bernard Carr, Florian Kühnel, and Marit Sandstad. Primordial black holes as dark matter. *Physical Review D*, 94(8):083504, 2016.

WD Cotton, K Thorat, JJ Condon, BS Frank, GIG Józsa, SV White, R Deane, N Oozeer, M Atemkeng, L Bester, et al. Hydrodynamical backflow in X-shaped radio galaxy PKS 2014-55. *Monthly Notices of the Royal Astronomical Society*, 495(1):1271–1283, 2020.

Christopher T Davies, Enrique Paillas, Marius Cautun, and Baojiu Li. Optimal void finders in weak lensing maps. *Monthly Notices of the Royal Astronomical Society*, 500(2):2417–2439, 2021.

I Delvecchio, E Daddi, MT Sargent, MJ Jarvis, D Elbaz, S Jin, D Liu, IH Whittam, H Algera, R Carraro, et al. The infrared-radio correlation of star-forming galaxies is strongly M-dependent but nearly redshift-invariant since $z \sim 4$. *Astronomy & Astrophysics*, 647:A123, 2021.

Mustafa Burak Dogruel, Xinyu Dai, Eduardo Guerras, Matthew Cornachione, and Christopher W Morgan. X-Ray Monitoring of Gravitationally Lensed Radio-loud Quasars with Chandra. *The Astrophysical Journal*, 894(2):153, 2020.

Chris L Fryer and Aimee Hungerford. Neutron Star Formation. In *The Electromagnetic Spectrum of Neutron Stars*, pages 3–14. Springer, 2005.

Alan H Guth. *The inflationary universe: the quest for a new theory of cosmic origins*. Random House, 1998.

MJ Hardcastle and JH Croston. Radio galaxies and feedback from AGN jets. *New Astronomy Reviews*, 88:101539, 2020.

Ian Harrison, Michael L Brown, Ben Tunbridge, Daniel B Thomas, Tom Hillier, AP Thomson, Lee Whittaker, Filipe B Abdalla, Richard A Battye, Anna Bonaldi, et al. SuperCLASS–III. Weak lensing from radio and optical observations in Data Release 1. *Monthly Notices of the Royal Astronomical Society*, 495(2):1737–1759, 2020.

George Helou, BT Soifer, and Mo Rowan-Robinson. Thermal infrared and nonthermal radio-Remarkable correlation in disks of galaxies. *The Astrophysical Journal*, 298:L7–L11, 1985.

Matt Hilton, Matthew Hasselfield, Cristóbal Sifón, Nicholas Battaglia, Simone Aiola, V Bharadwaj, J Richard Bond, Steve K Choi, Devin Crichton, Rahul Datta, et al. The Atacama Cosmology Telescope: the two-season ACTPol Sunyaev–Zel'dovich effect selected cluster catalog. *The Astrophysical Journal Supplement Series*, 235(1):20, 2018.

Edwin Powell Hubble. *The realm of the nebulae*. Yale University Press, 1936.

Karl G Jansky. A note on the source of interstellar interference. *Proceedings of the Institute of Radio Engineers*, 23(10):1158–1163, 1935.

Matt J Jarvis, David G Bonfield, VA Bruce, JE Geach, K McAlpine, RJ McLure, E González-Solares, M Irwin, J Lewis, A Kupcu Yoldas, et al. The VISTA deep extragalactic observations (VIDEO) survey. *Monthly Notices of the Royal Astronomical Society*, 428(2):1281–1295, 2013.

Matt J Jarvis, AR Taylor, I Agudo, James R Allison, RP Deane, B Frank, N Gupta, I Heywood, N Maddox, K McAlpine, et al. The Meerkat international GHz tiered extragalactic exploration (MIGHTEE) survey. *arXiv preprint arXiv:1709.01901*, 2017.

Arti Joshi, JC Pandey, Ashish Raj, KP Singh, GC Anupama, and HP Singh. Optical and X-ray studies of three polars: RX J0859. 1+ 0537, RX J0749. 1–0549, and RX J0649. 8–0737. *Monthly Notices of the Royal Astronomical Society*, 491(1):201–214, 2020.

Atoosa Kasirzadeh. ChatGPT, Large Language Technologies, and the Bumpy Road of Benefiting Humanity. *arXiv preprint arXiv:2304.11163*, 2023.

KI Kellermann, R Sramek, M Schmidt, DB Shaffer, and R Green. VLA observations of objects in the Palomar Bright Quasar Survey. *The Astronomical Journal*, 98:1195–1207, 1989.

KI Kellermann, JJ Condon, AE Kimball, RA Perley, and Željko Ivezić. Radio-loud and Radio-quiet QSOs. *The Astrophysical Journal*, 831(2):168, 2016.

MR Kennedy, RP Breton, CJ Clark, VS Dhillon, M Kerr, DAH Buckley, SB Potter, D Mata Sánchez, JG Stringer, and TR Marsh. Optical, X-ray, and $\gamma$-ray observations of the candidate transitional millisecond pulsar 4FGL J0427. 8-6704. *Monthly Notices of the Royal Astronomical Society*, 494(3):3912–3926, 2020.

Amy E Kimball, Kenneth I Kellermann, James J Condon, Željko Ivezić, and Richard A Perley. The two-component radio luminosity function of quasi-stellar objects: star formation and active galactic nucleus. *The Astrophysical Journal Letters*, 739(1):L29, 2011.

Marek J Kukula, James S Dunlop, David H Hughes, and Steve Rawlings. The radio properties of radio-quiet quasars. *Monthly Notices of the Royal Astronomical Society*, 297(2):366–382, 1998.

Mark Lacy and Anna Sajina. Active galactic nuclei as seen by the Spitzer Space Telescope. *Nature Astronomy*, 4(4):352–363, 2020.

Edward MacKinnon. De Broglie's thesis: A critical retrospective. *American Journal of Physics*, 44(11):1047–1055, 1976.

Natasha Maddox, Paul C Hewett, SJ Warren, and SM Croom. Luminous K-band selected quasars from UKIDSS. *Monthly Notices of the Royal Astronomical Society*, 386(3):1605–1624, 2008.

Andrea Merloni, Sebastian Heinz, and Tiziana Di Matteo. A Fundamental Plane of black hole activity. *Monthly Notices of the Royal Astronomical Society*, 345(4):1057–1076, 2003.

MJ Middleton, Piergiorgio Casella, Poshak Gandhi, E Bozzo, G Anderson, N Degenaar, I Donnarumma, G Israel, C Knigge, A Lohfink, et al. Paving the way to simultaneous multi-wavelength astronomy. *arXiv preprint arXiv:1709.03520*, 2017.

Neo Namane, Heba Sami, and Amare Abebe. Oscillating cosmological correlations in f(R) gravity. *arXiv preprint arXiv:1807.11330*, 2018.

P Padovani, V Mainieri, P Tozzi, KI Kellermann, EB Fomalont, N Miller, P Rosati, and P Shaver. The very large array survey of the Chandra Deep Field South. IV. Source population. *The Astrophysical Journal*, 694(1):235, 2009.

Francesca Panessa, Ranieri D Baldi, Ari Laor, Paolo Padovani, Ehud Behar, and Ian McHardy. The Origin of Radio Emission from Radio-Quiet AGN. *arXiv preprint arXiv:1902.05917*, 2019.

PF Roche, DK Aitken, CH Smith, and SD James. NGC 4418; a very extinguished galaxy. *Monthly Notices of the Royal Astronomical Society*, 218(1):19P–23P, 1986.

PR Roelfsema and RJ Allen. Radio observations of HI in UGC 2885, the largest identified SC galaxy. *Astronomy and Astrophysics*, 146:213–222, 1985.

Heba Sami, Neo Namane, Joseph Ntahompagaze, Maye Elmardi, and Amare Abebe. Reconstructing f(R) gravity from a Chaplygin scalar field in de Sitter spacetimes. *International Journal of Geometric Methods in Modern Physics*, 15(02):1850027, 2018.

Gregory A Shields. A brief history of active galactic nuclei. *Publications of the Astronomical Society of the Pacific*, 111(760):661, 1999.

Masato Shirasaki, Oscar Macias, Shin'ichiro Ando, Shunsaku Horiuchi, and Naoki Yoshida. Cross-correlation of the extragalactic gamma-ray background with the thermal Sunyaev-Zel'dovich effect in the cosmic microwave background. *Physical Review D*, 101(10):103022, 2020.

Joseph Simon. Exploring Proxies for the Supermassive Black Hole Mass Function: Implications for Pulsar Timing Arrays. *The Astrophysical Journal Letters*, 949(2):L24, 2023.

DH Sliney. What is light? the visible spectrum and beyond. *Eye*, 30(2):222–229, 2016.

Tristan L Smith, Marc Kamionkowski, and Asantha Cooray. Direct detection of the inflationary gravitational-wave background. *Physical Review D*, 73(2):023504, 2006.

Robert Stobie, Jacobus G Meiring, and David AH Buckley. Design of the Southern African Large Telescope (salt). In *Optical Design, Materials, Fabrication, and Maintenance*, volume 4003, pages 355–362. International Society for Optics and Photonics, 2000.

D Thomas, F Brimioulle, R Bender, U Hopp, L Greggio, C Maraston, and RP Saglia. A counter-rotating core in the dwarf elliptical galaxy VCC 510. *Astronomy & Astrophysics*, 445(1):L19–L22, 2006.

A Richard Thompson. Fundamentals of radio interferometry. In *Synthesis Imaging in Radio Astronomy II*, volume 180, page 11, 1999.

Sarah White. *Accretion and star formation in quasars*. PhD thesis, University of Oxford, 2015.

Sarah V White, Matt J Jarvis, Boris Häußler, and Natasha Maddox. Radio-quiet quasars in the VIDEO survey: evidence for AGN-powered radio emission at $s_{1.4}$ ghz $< 1$ mJy. *Monthly Notices of the Royal Astronomical Society*, 448(3):2665–2686, 2015.

Sarah V White, Matt J Jarvis, Eleni Kalfountzou, Martin J Hardcastle, Aprajita Verma, José M Cao Orjales, and Jason Stevens. Evidence that the AGN dominates the radio emission in $z \sim 1$ radio-quiet quasars. *Monthly Notices of the Royal Astronomical Society*, 468(1):217–238, 2017.

Min S Yun, Naveen A Reddy, and JJ Condon. Radio properties of infrared-selected galaxies in the IRAS 2 Jy sample. *The Astrophysical Journal*, 554(2):803, 2001.